Applied Catalysis B: Environment and Energy 384 (2026) 126194

Contents lists available at ScienceDirect

Applied Catalysis B: Environment and Energy

journal homepage: www.elsevier.com/locate/apcatb

Isoeugenol hydrodeoxygenation over sustainable biochar-supported cobalt catalysts: Synergistic Co^0/Co^{2+} sites and mechanistic insights

Lilia Longo [a,*], Dmitry Yu. Murzin [b,*], Davide Baldassin [a], Päivi Mäki-Arvela [b], Johan Wärnå [b], Anssi Peuronen [c], Matej Huš [d,e,f], Blaž Likozar [d], Atte Aho [b], Mark E. Martinez Klimov [b], Olha Yevdokimova [b], Kari Eränen [b], Mika Lastusaari [c], Michela Signoretto [a]

[a] Department of Molecular Sciences and Nanosystems Ca' Foscari University of Venice, Via Torino 155, Venezia 30172, Italy
[b] Åbo Akademi University, Johan Gadolin Process Chemistry Centre, Henriksgatan 2, Turku/Åbo 20500, Finland
[c] University of Turku, Department of Chemistry, Turku FI-20014, Finland
[d] National Institute of Chemistry, Department of Catalysis and Chemical Reaction Engineering, Hajdrihova 19, Ljubljana SI-1000, Slovenia
[e] University of Nova Gorica, Vipavska cesta 13, Nova Gorica SI-5000, Slovenia
[f] Association for Technical Culture of Slovenia (ZOTKS), Zaloška 65, Ljubljana SI-1000, Slovenia

ARTICLE INFO

Keywords:
Hydrodeoxygenation
Isoeugenol
Kinetic
Biochar
Cobalt
Reaction mechanism
DFT

ABSTRACT

This work demonstrates the potential of low-cost cobalt catalysts supported on activated biochars from biomass on the hydrodeoxygenation of isoeugenol, bio-oil model compound for the production of sustainable aviation fuels. Co/biochar catalysts were obtained by pyrolysis and steam activation of rice husk, leather waste, and their mixture, followed by metal impregnation, calcination, and reduction. Compared to Co/AC, (commercial active carbon), Co/A-RH, (rice husk biochar), exhibited competitive isoeugenol conversion to propylcyclohexane (PCH) at 300 °C, 30 bar, 4 h, with a higher initial rate (r_0PCH = 0.38 vs 0.34 mmol/min g_{Co}), but lower PCH yield (55 % vs 75 %), due to hydrocracking. By kinetic modeling, the activation energy for PCH formation was determined to be 151 kJ/mol. Comprehensive characterization revealed that Co^0-Co^{2+} synergy enhances HDO performance. DFT calculations provided mechanistic insight into the HDO pathways, which were consistent with the experimentally derived reaction network, and kinetic model.

1. Introduction

The transition to renewable energy is driven by the need to reduce reliance on fossil fuels, to mitigate greenhouse gas emissions [1]. The transport sector alone is responsible for nearly 23 % of global CO_2 emissions, with aviation contributing significantly [2,3]. Sustainable aviation fuels (SAF), derived from lignocellulosic biomass are considered promising solutions [3], with bio-oil from fast pyrolysis serving as a key feedstock [4,5]. In this thermochemical process, biomass is decomposed in the absence of oxygen, producing three fractions: a liquid (bio-oil), a solid (biochar), and a gaseous phase (biogas) [6]. The composition of bio-oil is highly complex, containing over 200 oxygenated compounds such as acids, aldehydes, ketones, furans, and phenolics [7]. These compounds impart poor stability, low energy density, and corrosiveness, rendering bio-oil unsuitable for a direct use as a fuel [8]. Hydrodeoxygenation (HDO) is therefore essential to improve fuel properties by removing oxygen mainly through hydrogenation and deoxygenation pathways [9–11]. The hydrogenation reactions are facilitated by a metallic phase (Pd [12,13], Pt [14,15], Ir [15], Ru [11,16–18], Ni [19–23], Cu [24–26], Co [27–32], Fe [33–35]) which is effective in saturating double bonds and enhancing stability of the reactive intermediates [36,37]. Among these, cobalt catalysts are particularly promising for HDO because of their oxophilicity, given by possible coexistence of cobalt in both metallic and oxide form [28,38–40], that enhances their interactions with oxygenated species, promoting effective C-O bond cleavage during HDO [25,38]. In addition, cobalt offers a lower cost compared to noble metals [41]. In addition to the metallic phase, oxyphilic compounds with acidic sites and oxygen vacancies are crucial for the deoxygenation reactions and cleavage of the C-O bonds (Fig. 1), as they promote dehydration, hydrogenolysis, and adsorption of oxygenated compounds [13]. For this reason, traditionally metal oxides such Al_2O_3 [42], SiO_2 [43], TiO_2 [11], CeO_2 [31], ZrO_2 [32] or highly ordered materials such as SBA-15 [23,30,32], and zeolites [44–46] have been used as supports. However, some of these

* Corresponding authors.
E-mail addresses: lilia.longo@unive.it, lilia.longo@abo.fi (L. Longo), dmurzin@abo.fi (D.Yu. Murzin).

https://doi.org/10.1016/j.apcatb.2025.126194
Received 23 September 2025; Received in revised form 8 November 2025; Accepted 11 November 2025
Available online 12 November 2025

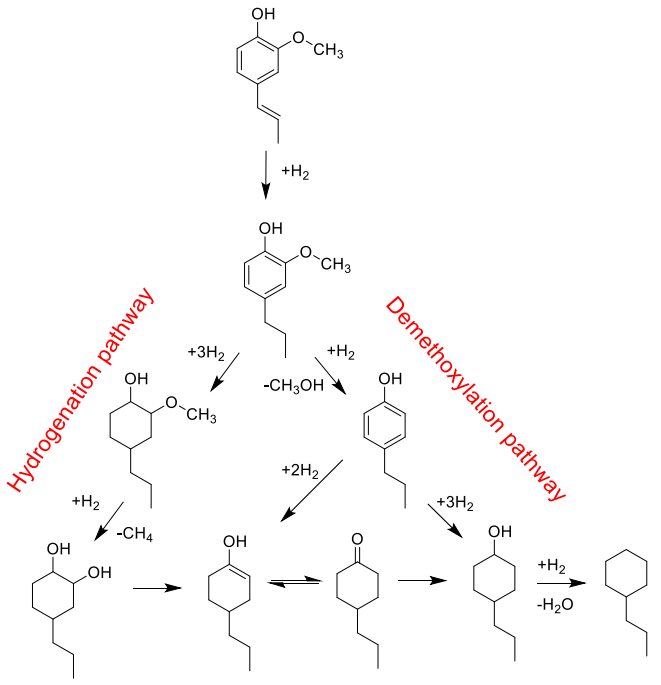

Fig. 1. Reaction scheme for transformation of isoeugenol to propylcyclohexane.

materials could suffer from hydrothermal instability, leading to catalyst deactivation, especially in the presence of water produced during HDO reactions [44]. Another important limitation concerns the high production cost of ordered mesoporous oxides and zeolites [47–49]. In the recent years, carbon-based supports have gained significant attention in HDO process due to their stability, tunable porosity, and large surface area, improving metal dispersion and reducing coke formation [18, 50–53]. Recently Chen et al. reported the use of carbon fibers as support for a Pt-based catalyst in a fixed-bed reactor for the selective dehydrogenation of methylcyclohexane, achieving a stability of 72 h [54]. An additional advantage is that carbonaceous material can be produced from renewable feedstocks, as biochar, the solid carbon-rich product obtained from biomass. Unlike conventional carbon materials from fossil precursors, biochar represents a renewable and low-cost alternative with distinctive surface chemistry and structural properties arising from its biomass origin and pyrolysis conditions [55,56]. Biochar typically contains oxygenated surface groups that can promote deoxygenation reactions [20], while its intrinsic hydrophobicity provides resistance to water formed during the reaction, helping maintaining catalyst activity over prolonged periods [20,50,55,57]. Several studies have demonstrated the superior performance of biochar-supported catalysts for HDO [58,59]. For example, Shu et al. [60] reported that ruthenium supported on biochar derived from bamboo, coupled with HSiW, showed higher catalytic activity and stability in the HDO of guaiacol, than commercial Ru/C + HSiW, due to the improved metal dispersion derived from the enhanced mesoporosity of bamboo-derived biochar.

Biochar can be produced from virtually any biomass; however, the feedstock strongly influences the final properties of the material, in terms of surface functionalities, porosity, and stability [61,62]. These physicochemical features can be further tailored through various treatment procedures such as, for example, steam activation, which increases the surface area and generates additional porosity [63,64]. For this reason, it is important to explore the potential use of different feedstocks, especially industrial byproducts, that can be upcycled and used as alternative catalytic materials, providing both environmental and economic benefits.

In this work, two waste feedstock was selected for the production of steam activated biochars: rice husks (A-RH), and shavings waste derived from a chromium-free leather tannery process (A-LS). The activated biochar obtained by the co-pyrolysis of such biomass (A-RL) was also considered, as previous investigations showed that combining the two precursors allows modulation of the resulting properties [65]. The choice of these feedstocks was motivated by several considerations: rice is the single most important crop, being a staple food for over half of the global population [66], while tannery industry generates large amounts of solid waste, up to 70 % of the initial leather mass [67]. Moreover, these types of biomass differ markedly in the chemical composition: rice husk is a lignocellulosic biomass rich of silica, whereas animal-derived leather shavings are rich in collagen and nitrogen-containing compounds. Consequently, their derived biochars exhibit distinct structural and surface properties, as previously reported [65]. The role of these activated biochars was investigated in combination with cobalt as the active metal phase for the HDO of iseoeugenol (IE). IE was selected as a representative bio-oil compound because its methoxy, hydroxyl, and propenyl groups make it an ideal probe for investigating the deoxygenation mechanisms relevant to bio-oil upgrading [68].

The use of Co catalyst in the HDO of complex molecules such as isoeugenol (IE) remains underexplored, and to date, no examples of Co supported on biochars for this specific reaction are reported in the literature. Lindfors et al. were the first to investigate Co supported on various oxides for the HDO of IE, finding Co/SBA-15 to be the most effective, with 63 % of propylcyclohexane (PCH) yield [30], however, SBA-15 is challenging to synthesize, requiring long preparation times, the use of templating agents that must be removed by calcination, which makes it costly and limits its large-scale application [47,48]. More recently, Li et al. [52] reported excellent performance using Co supported on nitrogen-doped carbon (Co/NC), for the same reaction, although the carbon support originated from the pyrolysis of a triazine-based polymer, which is less environmentally benign than the reuse of waste biomass. In contrast, biochar's renewable nature makes it a valuable offers a greener alternative, making it an attractive catalytic support for SAF production, contributing to the reduction of aviation's carbon footprint [56,69].

The HDO of IE proceeds through two main pathways: hydrogenation steps that saturate the allyl and aromatic moieties, and deoxygenation steps (demethoxylation and dehydroxylation) that remove oxygen functionalities. Understanding the interplay of these pathways is essential for controlling selectivity and minimizing undesired side reactions. The overall transformation of IE to propylcyclohexane (PCH), a valuable hydrocarbon for SAF production, is shown in Fig. 1 [70].

By exploring the intrinsic properties of carbon-based materials alongside the catalytic activity, product distribution, and stability of this system, this study aims to advance to the development of efficient and sustainable catalysts for bio-oil upgrading. Comprehensive material characterizations (TPR, NH_3TPD, XRD, XPS etc.) revealed the synergistic role of Co^0/Co^{2+} species in promoting HDO activity. Beyond catalysts screening, a kinetic study combined with density functional theory (DFT) calculations enabled the construction of a detailed reaction network and quantification of activation barriers. This integrated experimental-computational approach not only elucidates the reaction mechanism of IE HDO but also provides design principles for optimizing biochar-supported catalysts towards sustainable aviation fuel production.

2. Experimental

2.1. Catalyst preparation

10 wt% Co/biochar were prepared by wet impregnation. Three activated biochars, derived from rice husk (A-RH), leather shaving waste (A-LS) and the co-pyrolysis of the two biomasses (A-RL), were used as supports. As a reference, 10 wt% Co/AC was prepared, using

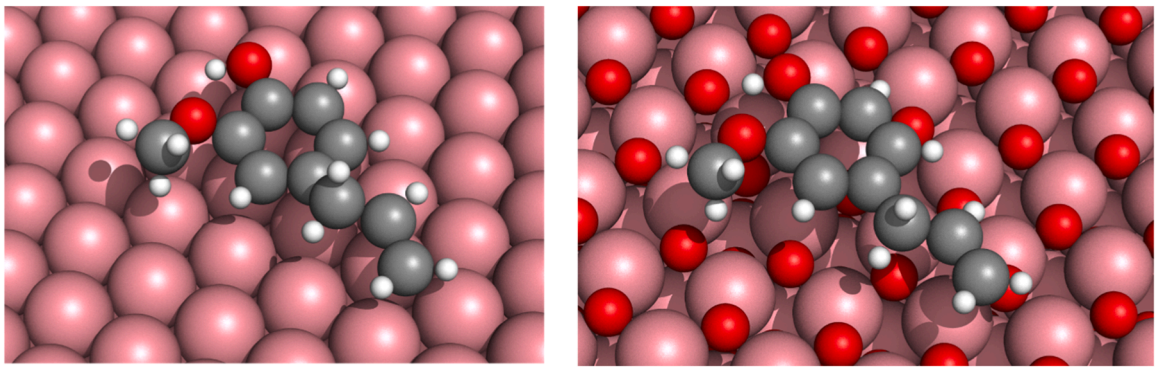

Fig. 2. The Co(0001) (left) and CoO(111) right models used in DFT calculations with one adsorbed isoeugenol molecule.

commercial activated carbon as support. The four catalysts were labelled Co/A-RH, Co/A-LS, Co/A-RL, and Co/AC, respectively. The proper amount of $Co(NO_3)_2 \cdot 6\ H_2O$ (Sigma Aldrich) was dissolved in 250 mL of distilled water and placed in a round bottom flask. 0,9 g of biochar were added to the solution. The suspension was kept under stirring at 70 °C for six hours to allow adsorption of the metal in the pores of the char. After six hours, water was removed by rotary evaporation and the catalyst was dried at 110 °C overnight. After that it was subjected to calcination under an inert atmosphere (argon) and reduction under H_2. The calcination and reduction temperatures were chosen after Temperature Programmed Desorption and Temperature Programmed Reduction analyses respectively, to evaluate the temperature of decomposition of nitrates and the reduction temperature of cobalt oxide. Calcination was conducted at 350 °C in Ar (40 mL/min, temperature program 10 °C/min, for 2 h). Reduction was conducted prior to every reaction, at 450 °C in H_2 (5 °C/min for 2 h).

2.2. Catalyst characterization

The metal content was measured by MP-OES (Perkin Elmer Optima 5300 DV Optical Emission Spectrometer), after digesting the catalyst (ca 50 mg) in a mixture of aqua regia (HCl:HNO_3 3:1) under microwave for one hour. The textural properties of the supports, and the fresh and spent catalysts were evaluated by N_2 physisorption at −196 °C (Micromeritics Tristar Plus II). The surface area was calculated by the BET method. Temperature-programmed desorption (TPD), reduction (TPR), and NH_3 desorption (NH_3TPD) were performed with Microtrac Belcat II equipment, coupled with mass spectrometer Pfeiffer Vacuum Omni Star. TPD was performed in He (30 mL/min) with a temperature ramp of 10 °C/min up to 100 °C for 30 min, 10 °C/min up to 800 °C for 20 min. TPR was performed using a mixture of 5 % H_2 in Ar (flow 30 mL/min) with a ramp temperature of 10 °C/min from 50 °C to 800 °C, after a pretreatment in Ar (30 mL/min) at 200 °C for 2 h. NH_3TPD was performed after a reduction step: first the sample was reduced by a 5 % H_2 in Ar mixture (30 mL/min) with a temperature ramp of 10 °C/min from 50 °C to 450 °C and kept at these conditions for two hours. The system was further cooled down to 100 °C, and a mixture of 5 % of NH_3 in He (30 mL/min) was exposed to the sample for 30 min, followed by purging in He (30 mL/min) for 60 min. The desorption was carried out in He (30 mL/min) with a temperature ramp of 10 °C/min up to 800°C. The final temperature was maintained for 20 min. Co particles size and distribution were evaluated by Transmission Electron Microscopy (TEM) using a JEM-1400 (voltage). The equipment used for analysis was a Model JEM-1400Plus system (JEOL, Japan) with a maximal acceleration voltage of 120 kV. Prior to the TEM analysis, the samples were ground and suspended in ethanol. A drop of suspension was mounted on a copper grid coated with a carbon film and the solvent was evaporated. The particle size distribution of metal particles was determined by measuring the diameter (d) of more than 300 particles visible in TEM micrographs. The size of the metal nanoparticles was measured by ImageJ software, and assuming the spherical shape, the dispersion was calculated as Eq.1 [71]:

$$D = \frac{6 * A}{\rho * \sigma * \quad N_A * d_{avg}} \quad x100 \tag{1}$$

where A = atomic mass, ρ = metal density, σ = average surface area occupied by one atom and N_A = Avogadro's constant. Powder X-ray diffraction measurements were performed by Panalytical Aeris Research Edition diffractometer in Bragg-Brentano geometry, using Cu Kα radiation and equipped with PIXcel1D detector, in the diffraction angle 2θ between 5° and 85°. The samples were first ground to powder using a zero-background silicon sample holder. X-ray photoelectron spectroscopy (Thermo Fischer Scientific, NEXSA XPS) was used to analyse the active metals on the fresh and spent catalysts. Al Kα radiation was used for the measurements with a spot size of 400 μm. The peak fitting was made with XPSPeak4.1 software, prior to peak fitting the Shirley background was subtracted from the data. C1s (284.8 eV) peak of the carbon support material was used as a reference peak to take possible sample charging into account.

2.3. Catalytic experiments

HDO experiments were carried out in a 300 mL semi-batch reactor (PARR Instruments), equipped with a mechanical stirrer. In a typical experiment the desired amount of the pre-reduced catalyst was added to the system together with 50 mL of dodecane (Sigma Aldrich), used as a solvent, and the proper amount of reactant/s. The catalyst particle size was maintained < 63 μm and the stirring 900 rpm, to avoid mass transfer limitations. The reaction was monitored by sampling the liquid at specific time intervals. Co/A-RH was also reused for three catalytic cycles. Prior to recycling, the catalyst was washed with acetone, dried in air, and reduced at the same conditions as before the first use. The liquid samples were analyzed by a gas chromatograph using a DB-1 capillary column (Agilent 122–103e, 30 m × 250 μm × 0.5 μm). The temperature program used for GC analysis was the following: 60 °C then 5 °C/min and 3 °C/min to 135 °C then 15 °C/min to 300 °C (1 min). The conversion, yield and selectivity were calculated upon calibration, using isoeugenol (cis + trans) (Sigma Aldrich), dihydroeugenol (≥99 %, Sigma-Aldrich), 4-propylcyclohexanone (> 98 % TCI), propyl cyclohexane (Sigma Aldrich). Conversion was calculated as Eq. 2:

$$Conversion(\%) = \left(\frac{mol_i \quad IE^* - \quad mol_t \quad IE^*}{mol_i \quad IE^*}\right) * 100 \tag{2}$$

* = or DHE

The products yield was calculated as Eq. 3:

$$Yield(\%) = \left(\frac{mol_t product}{mol_i \quad IE}\right) * 100 \tag{3}$$

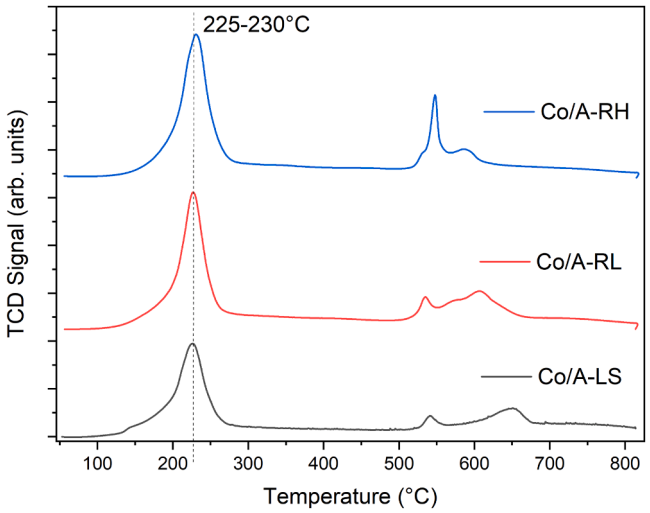

Fig. 3. TPD profiles of Co/A-RH (blue), Co/A-RL (red), and Co/A-LS (black).

The mass balance was calculated as Eq. 4:

$$Carbon\ balance(\%) = \left(\frac{mol_tIE + \Sigma mol_t products}{mol_iIE}\right) * 100 \quad (4)$$

2.4. DFT calculations

Density functional theory (DFT) calculations were performed as plane waves, as implemented in VASP 6.4.1. The electron-nuclei interactions were captured with the project augmented wave (PAW) approach. For well converged results, the wave function cut-off of 450 eV was considered sufficient. For electronic occupancies, a Gaussian smearing of 0.10 eV was used. An initial guess for the magnetic moment

Table 1
Textural properties of the supports and the catalysts.

Sample	S_{BET} (m^2g^{-1})	S_{micro} (m^2g^{-1})[c]	V_{tot} (cm^3g^{-1})[d]	V_{micro} (cm^3g^{-1})[e]
A-LS	633	789	0.25	0.23
Co/A-LS	434	528	0.19	0.15
A-RL	445	463	0.17	0.12
Co/A-RL	330	362	0.13	0.09
A-RH	367	543	0.14	0.10
Co/A-RH	214	173	0.11	0.07
AC	1113	1064	0.40	0.26
Co/AC	1010	823	0.32	0,14

aSurface area calculated by BET method. cMicropore surface area calculated by t-plot method. dTotal pore volume calculated according to the adsorbed amount of N2 and P/P0 values near 0.98. eMicropore volume calculated by t-plot method.

Table 2
Co loading determined by ICP-MS analysis, Co particle size and metal dispersion, measured by TEM, and S_{BET} determined by N_2 physisorption.

Sample	Cobalt wt%	d_{TEM} (nm)	D_{TEM} (%)
Co/A-LS	8	9.6 ± 0.8	57.8
Co/A-RL	13	8.9 ± 0.2	62.3
Co/A-RH	12	8.9 ± 0.2	62.3
Co/AC	16	8.2 ± 0.2	67.6

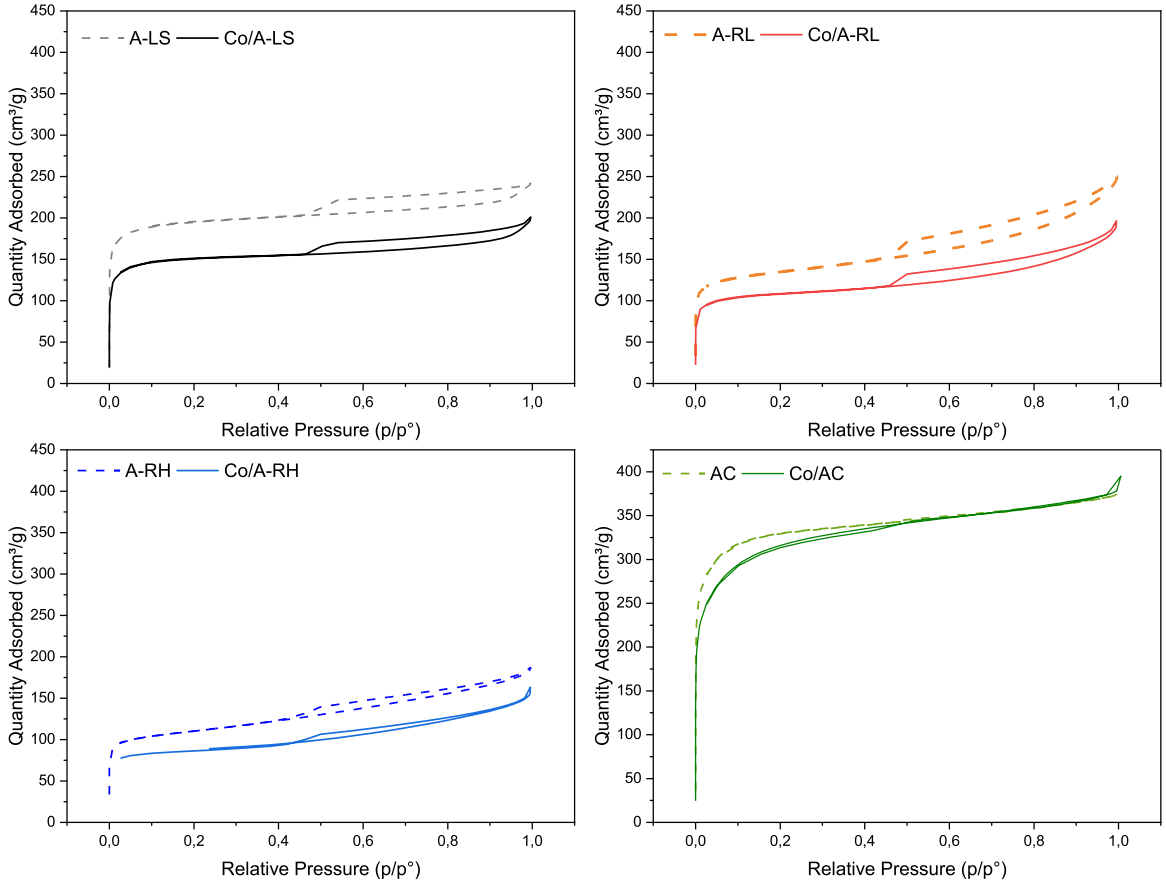

Fig. 4. N_2 adsorption-desorption isotherms of the supports (dotted lines) and the catalysts (solid lines).

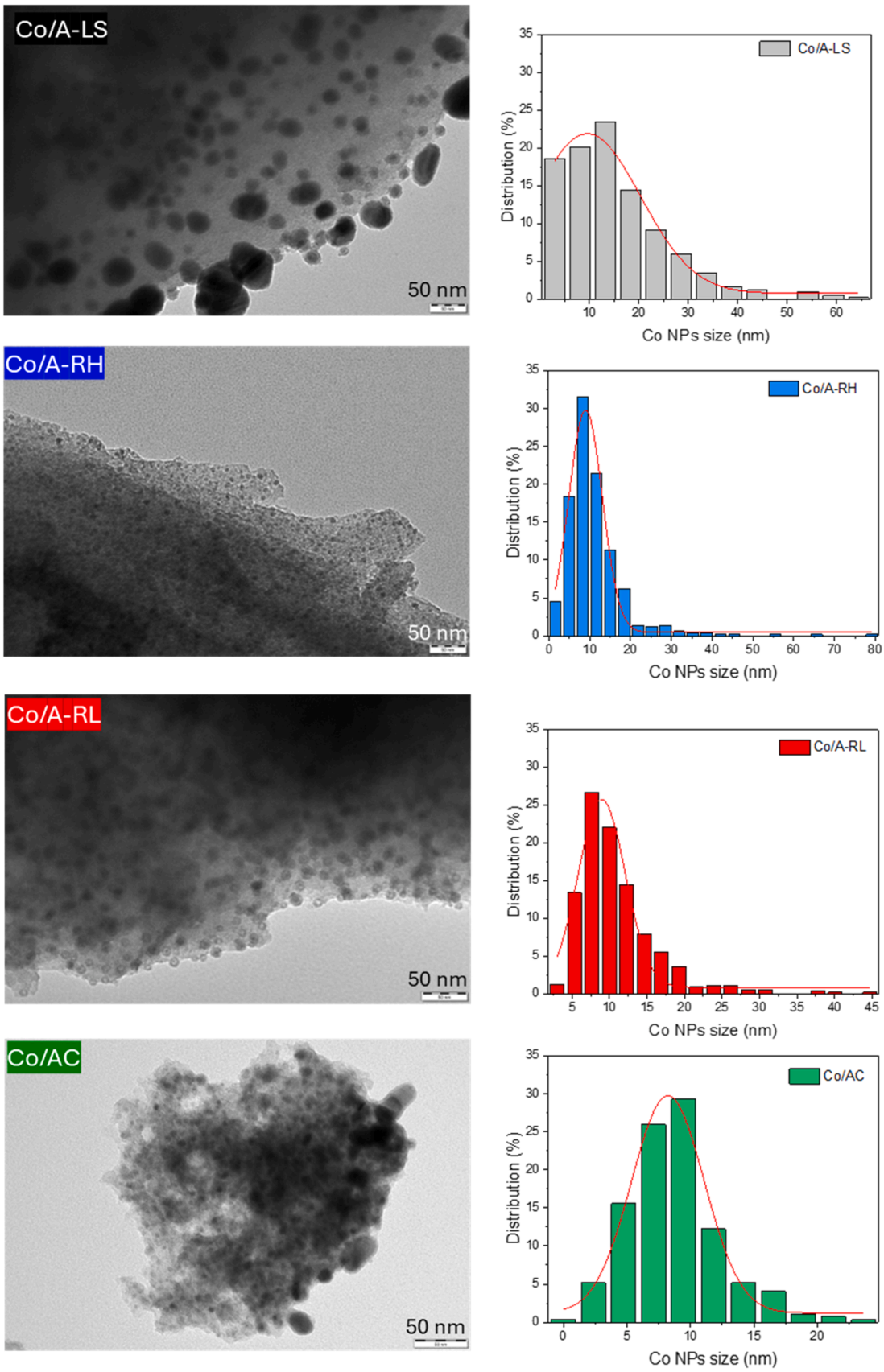

Fig. 5. TEM microscopy and NPs size distribution of the catalysts.

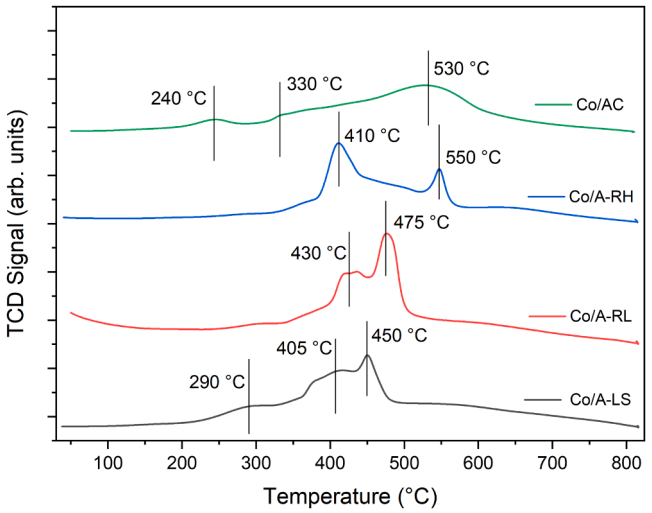

Fig. 6. TPR profiles of Co/A-RH (blue), Co/A-RL (red), Co/A-LS (black), and Co/AC (green).

Table 3
TPR results of different catalysts.

Catalyst	$T_{1,\ max}$ (°C)	$T_{2,\ max}$ (°C)	$T_{3,\ max}$ (°C)	Relative total peak area normalized by catalyst mass
Co/AC	240	330	530	0.61
Co/A-RH	n.a.	410	550	0.47
Co/A-RL	n.a.	430	475	0.96
Co/A-LS	290	405	450	1

of Co of 1.7 was used in the spin-polarized calculations. Standard dipole corrections and Grimme D3 van der Waals corrections were employed. Due to the unit cell size, the Brillouin zone was sampled at a gamma point only. The catalyst was modelled as a Co(0001) slab of four layers, bottom two being frozen in their bulk positions (Fig. 2). These were identified according to a hcp unit cell with constants of a = 2.476 Å, c = 4.055 Å, α = β = 90°, and γ = 120° during the bulk geometry optimization (with 8x8x8 K-point mesh). For Co 2 + species, a CoO(111) slab of four layers was modelled. The unit cell was optimized to constants of a = b = 3.011 Å, c = 7.320 Å, α = β = 90°, and γ = 120. To accommodate larger adsorbates and prevent spurious inter-cell interactions, the computations used 6 × 6 supercells with 12 Å of vacuum in the *z* direction. A force threshold of 0.01 eV/Å was used as a convergence criterion in the geometry optimizations of stable intermediates and transition states. The latter were identified using the dimer method and confirmed with the vibrational analysis, which proved precisely one imaginary frequency. For larger adsorbates, such as isoeugenol, we studied different positions on the surface were studied. Adsorption energies were calculated as Eq. 5:

$$E_{ads} = E_{structure} - E_{catalyst} - E_{adsorbate} \quad (5)$$

where $E_{structure}$ is the total energy of the structure with catalyst and adsorbed species, $E_{catalyst}$ is the total energy of empty catalyst and $E_{adsorbate}$ is the total energy of the adsorbate in vacuum. Similarly, the reaction energy and activation barriers were defined as Eq. 6:

$$\Delta E_{ads} = E_{final} - E_{initial} \text{and} E_a = E_{TS} - E_{initial} \quad (6)$$

For elementary reactions involving more than one reactant or product, they were considered adsorbed in separate cells to ensure thermodynamic consistency regardless of the pathway ($E_1 + E_2 - E_{catalyst}$).

3. Results

3.1. Catalysts characterization

TPD analyses were performed to evaluate the decomposition temperature of $Co(NO_3)_2$. In Fig. 3, the TPD profiles of the three biochar-based catalysts are reported.

For all samples, a primary peak centered between 225 and 230 °C is observed, along with two smaller peaks at higher temperatures (550–650 °C). Mass spectrometry analysis indicates that the first peak corresponds to the release of NO, H_2O, CO_2, CO, N_2, and O_2, suggesting the decomposition of nitrates. The higher temperature peaks are associated with the release of CO and CO_2, indicative of the decomposition of the char's functional groups. Based on these results, a calcination temperature of 350 °C was selected to ensure complete decomposition of the metal precursor. For all samples, calcination was performed under an inert atmosphere (Ar flow).

The textural properties of the catalysts were evaluated and compared to the pristine support by N_2 physisorption analysis (Fig. 4, Table 1). The results demonstrated that the porous structure of the biochars was preserved across all catalysts. The isotherms exhibited characteristics of both Type I and Type IV, indicating the presence of both micropores and mesopores, respectively, with an H4 hysteresis loop, which is typical of narrow slit-like pores in activated carbons [72]. However, cobalt impregnation led to a notable reduction in total surface area, likely due to pore blockage by the metal. The most significant surface area reduction, a 44 % decrease, was observed for Co/A-RH, suggesting a more uniform distribution of the metal across the surface of the material.

ICP-MS measurements (Table 2) indicated that Co/A-RH and Co/A-RL retained a higher metal loading (12 wt% and 13 wt% respectively) compared to Co/A-LS (8 wt%). The enhanced metal retention of A-RH and A-RL with respect to A-LS is attributed to their intrinsic morphology and microstructure, as reported in a previous work [65] (more information about the chemical composition and the morphology of the materials is reported in the Supporting Information, Fig. S1, Table S2). These characteristics likely facilitated more efficient cobalt deposition and interactions with the support, contributing to the higher metal loading observed. Notably, the amount of effective Co measured for Co/AC was the highest, being 16 wt%. This was particularly attributed to a very high surface area of this material (1113 m^2/g).

The particle size and distribution of metal particles on the catalysts, as shown in Table 2, were determined by Transmission Electron Microscopy (TEM) analysis (Fig. 5). All catalysts exhibited average particle diameters below 10 nm with a similar dispersion range (D_{TEM} 58–68 %) with the highest distribution on Co/AC, followed by Co/A-RH and Co/A-RL. Despite a high surface area, the Co/A-LS catalyst displayed a broader particle size distribution, including agglomerates larger than 50 nm, indicating poor interactions between the metal and the support.

Temperature Programmed Reduction (TPR) was conducted to evaluate the reducibility of the cobalt species (Fig. 6, Table 3). Fig. 6 presents the TPR profiles of the three biochar-based catalysts, and the comparison with Co/AC. The major reduction events, corresponding to the reduction of cobalt oxide (CoO) to metallic cobalt (Co°), occur between 400 °C and 600 °C across all samples. Both Co/A-LS (black curve) and Co/AC (green curve) show initial reduction peaks at 290 °C and 240 °C, respectively, which are typically attributed to the reduction of Co_3O_4 to CoO [73], indicating a higher oxidation tendency for Co for Co/A-LS and Co/AC. In the case of Co/AC (green curve), the primary reduction event is characterized by a broad peak that begins at 330 °C and centers around 550 °C. In contrast, the biochar-based catalysts exhibited two main reduction peaks. These peaks were partially overlapping for Co/A-LS (black curve, 405–450 °C) and Co/A-RL (red curve, 430–475 °C), while in Co/A-RH (410–550 °C) they appeared more distinct and well-separated.

The differences in peak profiles and temperatures suggest that the nature of the support significantly influences the reducibility of cobalt

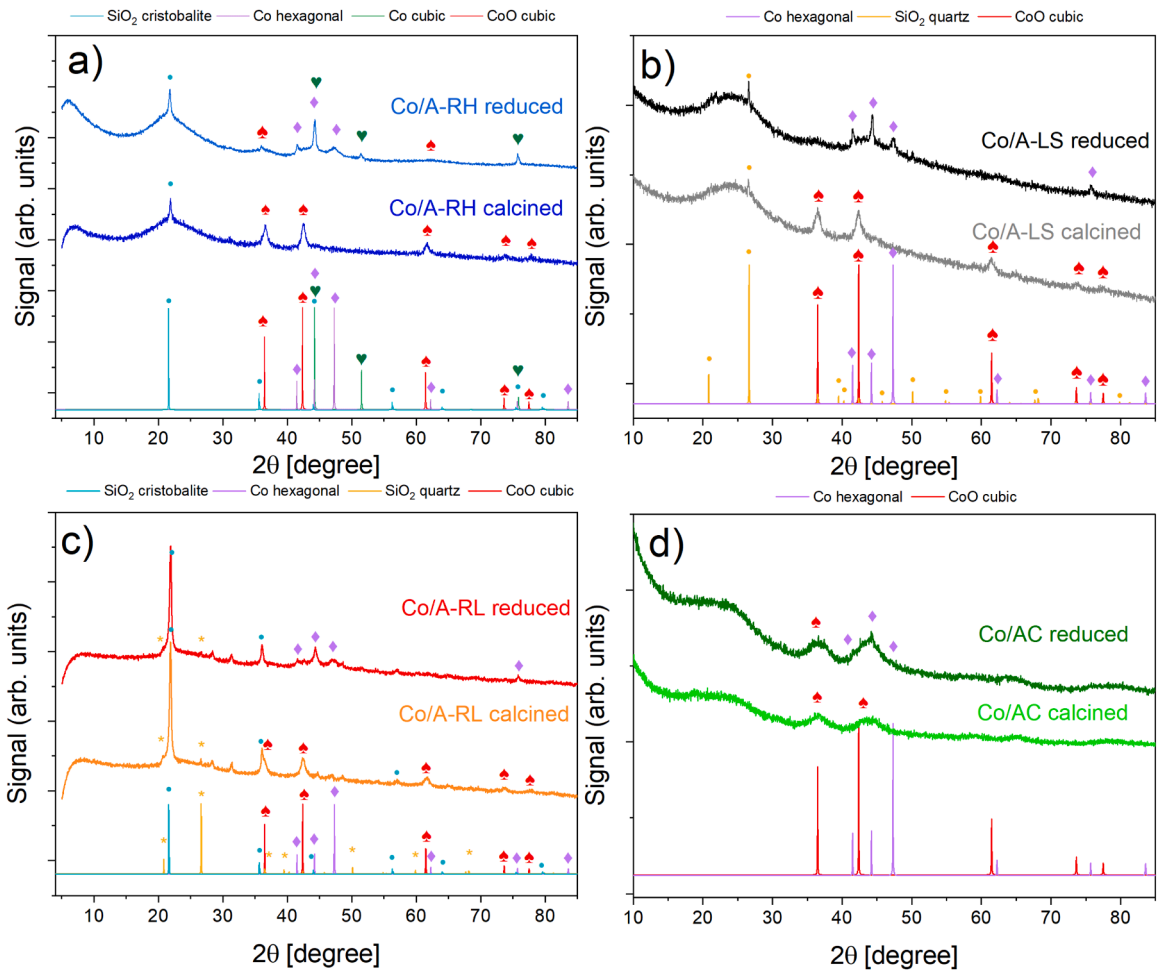

Fig. 7. XRD patterns of the catalysts before and after reduction. b) Co/A-RH, b) Co/A-LS, c) Co/A-RL, d) Co/AC.

oxides. The nature of this reduction event was unveiled by XRD analysis before and after reduction, to identify the resulting cobalt phases (Fig. 7). The reduction temperature was set at 450 °C for all samples.

According to data from the Crystallography Open Database (COD) files, distinct diffraction patterns corresponding to the support and metal phases were observed. All catalysts exhibited a similar amorphous phase peak at $2\theta = 23°$, which is attributed to the sp^2-hybridized graphitic carbon (002) crystalline phase. In all samples, signals corresponding to the silica phase were clearly present. The silica derived from rice husk predominantly exists in the form of cristobalite, while the silica in A-LS is mainly quartz. In the A-RL samples, reflections characteristic of both cristobalite and quartz are evident. No evidence of SiO_2 signal was detected on Co/AC, in line with the low ash content (Table S2). For all the calcined catalysts (represented by the blue, orange, gray, and light green curves), the diffraction peaks associated with cobalt indicated the formation of a face-centered cubic (fcc) structure of CoO. The characteristic diffraction peaks at 36.3°, 42.3°, 61.5°, 73.4°, and 77.2° correspond to the (111), (200), (220), (311), and (222) planes of CoO, respectively [38,74]. After reduction, the Co/A-LS and Co/A-RL catalysts exhibited complete reduction of Co(II) to Co(0), forming a hexagonal close-packed (hcp) structure. The characteristic diffraction peaks for the hcp phase were observed at 41.7° (100), 44.5° (002), and 47.5° (101). In contrast, the Co/A-RH catalyst exhibited the coexistence of both hcp and fcc phases of metallic cobalt, as indicated by a low-intensity diffraction peak at 51.5°, corresponding to the (111) plane of the fcc Co structure. Additionally, a minor contribution from the oxide phase was detectable in this sample [75]. A significant contribution from the oxide phase was observed in the reduced Co/AC sample. These findings align with TPR measurements (Fig. 6), suggesting that the support influenced the reducibility of the cobalt phase, resulting in only a partial reduction of Co for both Co/A-RH and Co/AC.

The surface chemical composition of the catalysts was investigated by XPS. The deconvoluted Co 2p spectra are shown in Fig. 8, while the corresponding binding energies and relative atomic percentage of cobalt species are summarized in Table 4. The C 1 s and O 1 s binding energies are reported in Table S1. The fitting of the Co2p region was done by first subtracting the Shirley background from the data. All catalysts exhibited a major peak (781.1 eV), along with the characteristic satellite peak (786.6 eV), corresponding to the Co^{2+} [76], and a minor peak (~ 778.8 eV) corresponding to the metallic Co^0 [38]. Notably, the atomic ratio between Co^0 and Co^{2+} followed the order Co/A-LS > Co/A-RL > Co/A-RH > Co/AC. It should be noted that during the preparation of the samples for XPS analysis, exposure to air led to partial surface passivation. Therefore, a higher proportion of metallic cobalt is expected under reaction conditions [28]. Nevertheless, the Co^0/Co^{2+} ratio follows the same trend observed in the XRD results: the samples with a higher Co^0 content, namely Co/A-LS and Co/A-RL, showed only the metallic phase in XRD. Conversely, Co/A-RH and Co/AC, which showed a lower amount of Co^0 by XPS, exhibited CoO reflections in XRD. This consistency suggests that the presence of metallic cobalt detected by XPS correlates well with the crystalline phases identified by XRD.

Given the documented cooperative effect between Co^0 and Co^{2+} species, acting respectively as hydrogenation and acid sites [38,77], the acidity of the catalysts was evaluated by NH_3-TPD. The desorption profiles are shown in Fig. 9, with the numerical values collected in Table 5.

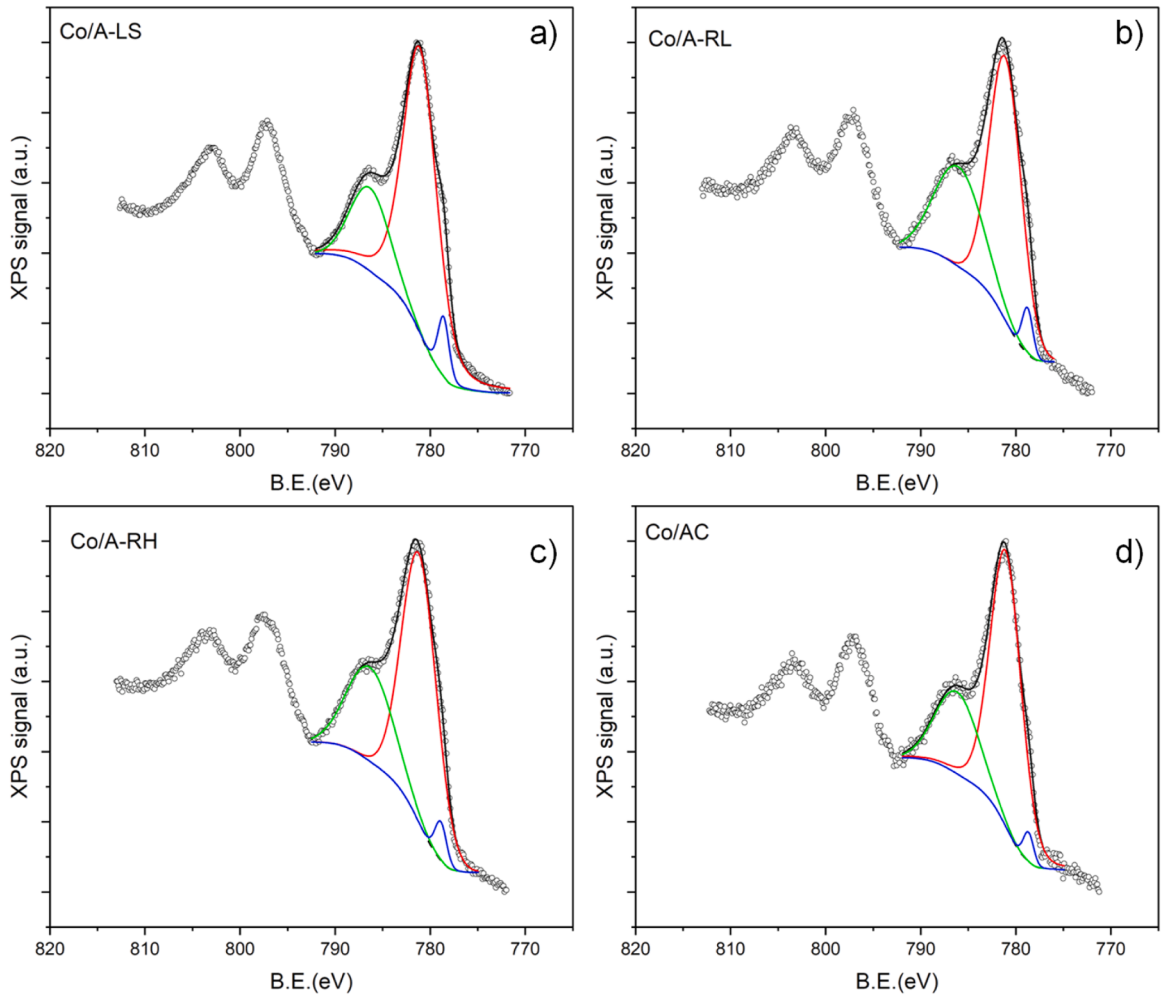

Fig. 8. Deconvoluted Co 2p spectra for a) Co/A-LS, b) Co/A-RL, c) Co/A-RH, d) Co/AC.

Table 4
XPS results of Co 2p signals for the different catalysts.

	Co/A-LS		Co/A-RL		Co/A-RH		Co/AC	
	BE (eV)	AC (at%)	BE (eV)	AC (at%)	BE (eV)	AC (at%)	BE (eV)	AC (at%)
Co 2p	781.1	93.8	781.1	94.5	781.1	95.4	781.1	96.8
	778.6	6.2	778.8	5.5	778.9	4.6	778.7	3.2

All biochar-based catalysts exhibited a broad desorption peak around 150 °C, indicative of weak acid sites. In Co/AC, this peak shifted to higher temperatures (around 245 °C). Co/A-RH (represented by the blue curve) displayed two sharp peaks centered at 455–470 °C, while Co/AC showed a broad peak at high temperatures, starting at 330 °C and centered at 535 °C. In contrast, this peak was almost absent in Co/A-LS and Co/A-RL. This observation indicates the presence of medium to strong acid sites in significant concentrations only for Co/A-RH and Co/AC. Comparison with the NH_3TPD of the catalysts with the ones of the bare support (Fig. S2) revealed no evident desorption signals can be attributed to the support themselves. Therefore, the acidity observed in Co/AC and Co/A-RH was attributed to the presence of CoO, which was absent in the other catalysts, as confirmed by XRD analysis (Fig. 7). The Co^{2+} species in CoO infer Lewis acidity, likely due to the electronic deficiency of the cobalt cations [38]. These comprehensive characterization results clearly demonstrate that the nature of the support significantly influences the metal distribution, metal-support interactions, and the oxidation state of the metal, that can determine the overall activity of the material, as will be discussed below.

3.2. *Isoeugenol HDO*

3.2.1. *Preliminary experiments*

HDO preliminary experiments were conducted using different catalyst-to-reactant ratios to verify whether the reaction occurred under kinetic control. The concentration of IE was kept constant at 2 mg/mL, while the amount of Co/A-RH catalyst was varied (20, 50, 80 mg). The results are reported in the Supporting Information (Fig. S3, S4, S5).

3.2.2. *Screening of the catalysts*

The catalytic performance of Co/A-LS, Co/A-RH, Co/A-RL, and Co/AC in the hydrodeoxygenation (HDO) of isoeugenol (IE) was evaluated at 300 °C under 30 bar hydrogen, using an initial IE concentration of 2 mg/mL and 50 mg of the catalyst (Table 6, Fig. 10). Due to different Co loadings, the conversion and yield percentages were plotted against normalized time, calculated by multiplying the reaction time by the

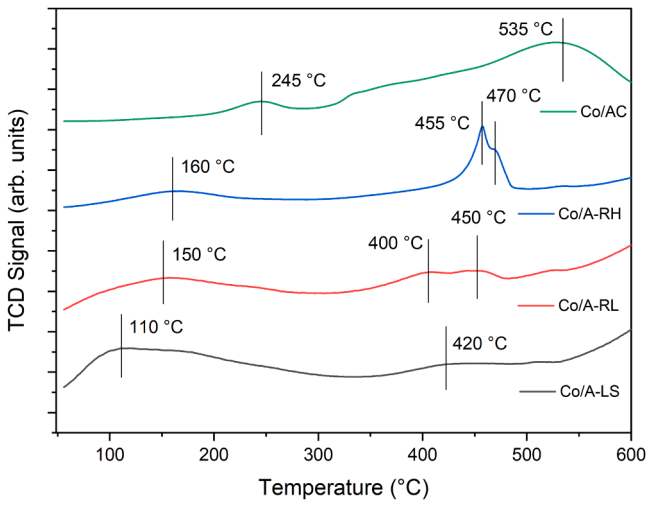

Fig. 9. NH_3 TPD profiles of Co/A-LS (black curve), Co/A-RL (red curve), Co/A-RH /blue curve), Co/AC (green curve).

Table 5
Results from NH_3TPD of the catalysts.

Catalyst	$T_{1,\ max}$ (°C)	$T_{2,\ max}$ (°C)	$T_{3,\ max}$ (°C)	Relative total peak area normalized by catalyst mass
Co/AC	245	n.a.	535	0.78
Co/A-RH	160	455	470	1.0
Co/A-RL	150	400	450	0.87
Co/A-LS	110	420	n.a.	0.76

mass of metal in each catalyst. This normalization enabled a more accurate comparison of catalytic activity and selectivity among the tested catalysts.

Over all the catalysts, hydrogenation of the double bond in the allyl chain of IE proceeded rapidly, leading to formation of dihydroeugenol (DHE) (Fig. 10). Due to the fast reaction kinetics, it was not feasible to monitor the conversion of IE to DHE [30]. Consequently, the study was focused on tracking the conversion of DHE over time to assess the catalytic performance of the catalysts. The initial rate for DHE transformation followed the order: Co/A-RH > Co/AC > Co/A-LS > Co/A-RL (Table 6). For Co/A-LS, the transformation rate declined after 30 min, while the other catalysts remained highly active, achieving 100 % DHE conversion. The initial DHE conversion rate correlated with the catalytic acidity, as the catalysts with strong acid sites exhibited higher activity. The most active catalyst (Co/A-RH) predominantly contained medium to strong acid sites, and the second most active (Co/AC), had the highest fraction of very strong acid sites (Table 5).

Multiple consecutive reactions were observed occurring over time: demethoxylation of the -OCH_3 group and hydrogenation of the aromatic were rapid, with 4-propylcyclohexanol (PCOL) emerging as the main product within the first hour of reaction. In parallel, 4-propylcyclohexanone (PCONE) was also detected, though it remained at low concentrations. PCOL was further converted into propylcyclohexane (PCH), with a clear trend observed for the most active catalysts, Co/A-RH and Co/AC. Co/A-RH demonstrated the highest activity, achieving complete conversion of DHE within 1 min and nearly complete conversion of PCOL to PCH within 240 min, with a maximum yield of 55 %. However, Co/A-RH showed lower PCH yield compared to Co/AC (75.5 %), due to a lower carbon balance (57.5 % Co/A-RH vs 75.2 % Co/AC). This difference was primarily attributed to a more pronounced occurrence of hydrocracking side reactions in presence of Co/A-RH, due to a more pronounced acidity. Evidence for these reactions was detected in the liquid phase, as shown in the chromatograms (Fig. S6 a-d), recorded at 300 °C and 30 bar. When comparing the chromatograms recorded after 1 and 240 min, several new peaks appear as the reaction progresses. Based on GC–MS analysis, these new peaks were identified as various hydrocarbons, confirming that hydrocracking occurred during the process. The chromatograms of Co/A-RH (Fig. S6 a,b) show much more intense signals than the ones of Co/AC (Fig S6 c,d), and some small, unidentified peaks at low retention time, attributed to lighter hydrocarbons, are visible in figure S6b but absent in Figure S6d suggesting a lower degree of hydrocracking with Co/AC. Although some of these species may also originate from the solvent (dodecane), and indeed, the possibility of co-processing fossil feedstocks with biomass-derived compounds has been previously reported [33], it cannot be excluded that also PCH, being an hydrocarbon itself, could undergo to hydrocracking. Notably, as it will be discussed in Section 3.4.1 and reported in Table 8, when the temperature was decreased to 275 °C, the carbon balance for Co/A-RH exceeded 95 % and the corresponding chromatograms (Fig. S6 e,f) displayed less pronounced peaks associated with hydrocracking products. Nevertheless, other side reactions, such as coking or polymerization, cannot be entirely excluded as contributing factors to the reduced mass balance. These aspects will be further discussed in Section 3.5 Catalyst recyclability. It is worth noting that the relation between acidity and carbon balance in this type of reaction has been already reported in literature. For instance, in the HDO of isoeugenol over Pt-Beta zeolites, the sum of the liquid phase products decreased with increasing acidity [46]. In addition, it was reported in HDO of isoeugenol over Pt-Re/carbon catalysts that the liquid phase mass decreased when pH of the catalyst slurry was ca. 6, while those with a higher pH gave a nearly complete liquid phase mass balance [14].

PCH yield decreased in the following order: 75.2 % (Co/AC) > 55.1 % (Co/A-RH) > 28.1 % (Co/A-RL) > 6.3 % (Co/A-LS) (Table 5). Similarly, TEM analysis revealed that the average metal particle size of these catalysts increased in the same order (Table 2), indicating higher hydrodeoxygenation activity with more dispersed catalysts. Moreover, the ratio between Co^0 and Co^{2+} increased following the same order, as confirmed by XRD and XPS analyses (Figs. 7 and 8). This increase was correlated to a decrease of acidity, as evidenced by NH_3TPD (Fig. 9), indicating that the coexistence of Co^0 and Co^{2+} species, and therefore metallic and acid sites, is beneficial to improve the adsorption and activation of oxygenated compounds, and promote C-O [38,78,79].

The Co^{2+} species, present as CoO nanoparticles with structural

Table 6
Results of the catalyst screening. Initial rates for DHE disappearance and PCH formation; DHE conversion and product yields at 240 min.

Entry	Initial rate for DHE disappearance (mmol/min g_{Co})	Initial rate for PCH formation (mmol/min g_{Co})	DHE Conversion (%)	PCONE Yield (%)	PCOL Yield (%)	PCH Yield (%)	C balance (%)
Co/A-LS	0.68	0.05	86.2	5.5	20.0	6.3	45.4
Co/A-RL	0.77	0.06	100	8.8	24.0	28.1	60.9
Co/A-RH	Large	0.38	100	0.7	1.7	55.1	57.5
Co/AC	1.68	0.34	100	0	0	75.2	75.2

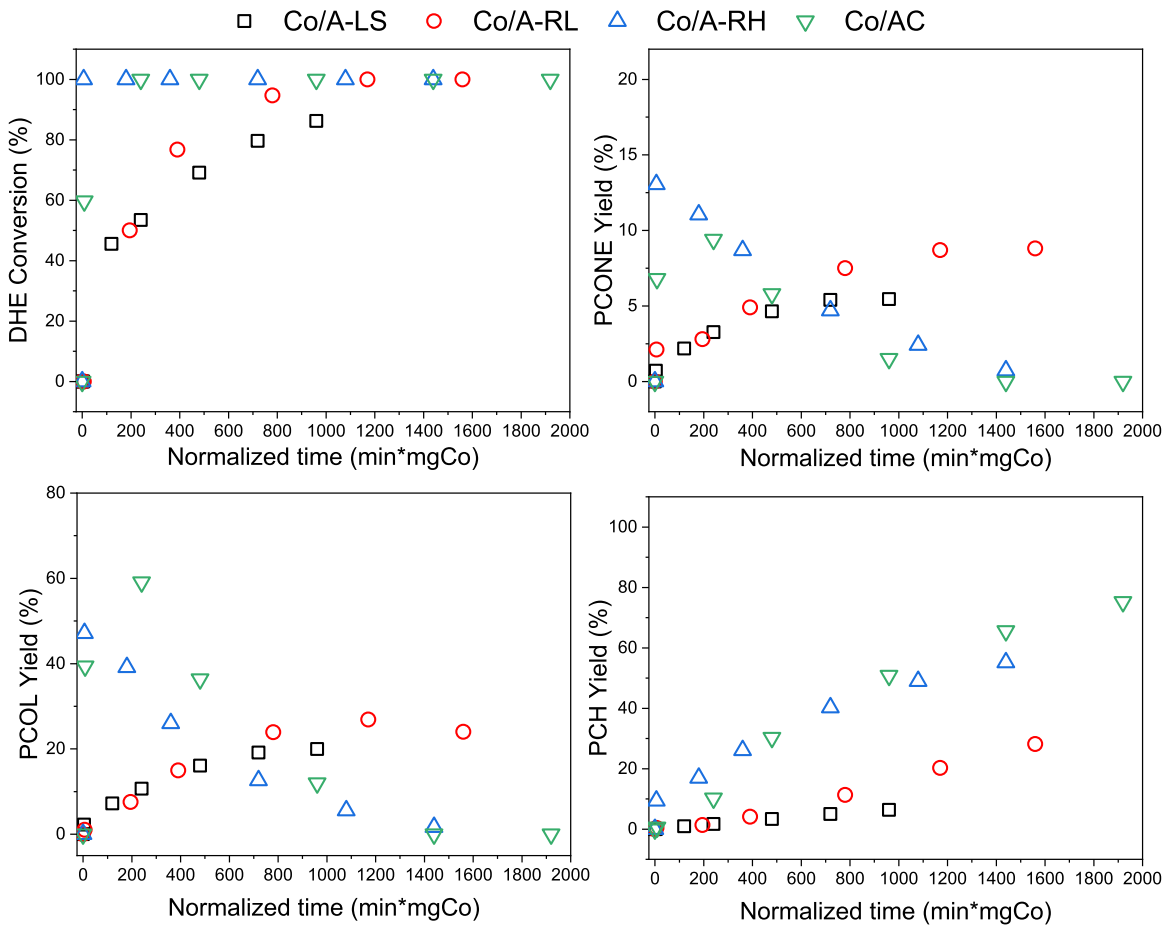

Fig. 10. Reaction profiles of isoeugenol HDO over different catalysts. Reaction conditions: IE 2 mg/mL, dodecane 50 mL, 50 mg cat., 300 °C, 30 bar H_2, 900 rpm, 240 min.

defects, play a crucial role in coordinating oxygenated compounds. These CoO nanoparticles contain oxygen vacancies that activate the C–O groups [39]. Moreover, CoO with oxygen vacancies is a highly active species for the heterolytic cleavage of H_2 [40]. As discussed in the introduction, the synergistic effect of metallic cobalt and CoO in HDO is well-documented. For example, Singh et al. highlighted that oxygen vacancies formed on Co/CoO catalysts, derived from Co_3O_4 reduction, were pivotal for the demethoxylation of guaiacol [80]. Using this system, the authors achieved 99 % conversion with 80 % selectivity toward cyclohexanol, at 180 °C 20 bar H_2. Similar results were reported by Wen et al. using Co/CeO_2, leveraging the oxygen vacancies provided by the support [31]. Additionally, Tian et. al. [29], demonstrated that CoOx was the active site for the hydrogenation of furfural, yielding cyclopentanone and cyclopentanol as the main products with a total yield of 82 %. In bimetallic CoNi, the presence of CoOx species lead to the formation of oxygen vacancies, improving catalytic performance on HDO of vanillin, yielding 100 % methyl cyclohexanol at mild conditions (200 °C, 1.0 MPa H_2) [79]. Similar synergy was found in CuCoOx catalysts for the HDO of 5-hydroxymethyl furfural to dimethylfuran [24].

Further evidence of the synergistic effect between the two cobalt oxidation states was obtained by comparing the catalytic activity of Co/A-RH in its reduced form with that of Co/A-RH in its calcined form, without an additional reduction step (Fig. 11). At 250 °C and 30 bar, the reaction proceeded at a slower rate with the calcined Co/A-RH catalyst. This resulted in a decrease in DHE conversion from 100 % to 72 %, as well as a lower yield of PCOL (from 79 % to 50 %) and PCH (from 5.3 % to 2.0 %) as the main products. Therefore, a balanced ratio of metallic Co and CoO species and an appropriate number of acid sites are necessary to prevent over-reactions, such as cracking, as observed for Co/A-RH.

The catalytic performance of the two best-performing catalysts from this study was compared with the results reported in the literature. Numerous studies have investigated the HDO of various phenolic compounds, such as guaiacol, phenol, and anisole, utilizing both noble and non-noble metal catalysts supported on various oxides, zeolites, and carbon materials. However, the focus of this work was primarily on the use of carbon-based supports and non-noble metals for the complete HDO of eugenol or IE to PCH. A comprehensive overview of the relevant literature data, particularly on carbon-supported and non-noble metal catalysts for HDO reactions, is provided in Table 7.

The PCH yields obtained using Co/A-RH and Co/AC catalysts in this study (55 % and 75 %, respectively) are competitive with other non-noble metal systems, such as Ni/graphite (60 %, Table 7 entry 3) and Co/SBA (63 %, Table 7 entry 9) [30]. These yields are also comparable to those achieved with some noble metal catalysts, including Pd/C + HZSM-5 (64 %, Table 7 entry 7) [83], Ru/C + Nb_2O_5 (74 %, Table 7 entry 5) [81], RuRe/MWCNT (63 %, Table 7 entry 4) [18]. Notably, the Pt/AC catalyst exhibits low yield of 25 % (Table 7 entry 1) [7], with propyl guaiacol resulting the main product, suggesting that noble metals often require the addition of oxophilic sites to enhance their performance in HDO reactions. Some noble metal catalysts, such as Ru/CNT, achieved a high PCH yield of 94 % (Table 7 entry 6) [82] likely due to the combination of well-dispersed Ru on supports with a high surface area, mechanical strength, and good chemical stability, resulting in enhanced metal-support interactions and a higher density of active sites. Among cobalt-based catalysts, the study by Lindfors et al. [30] showed that Co/SBA-15 was the most efficient catalyst producing PCH, while other supports like Co/SiO_2, Co/TiO_2, and Co/Al_2O_3 achieved yields of

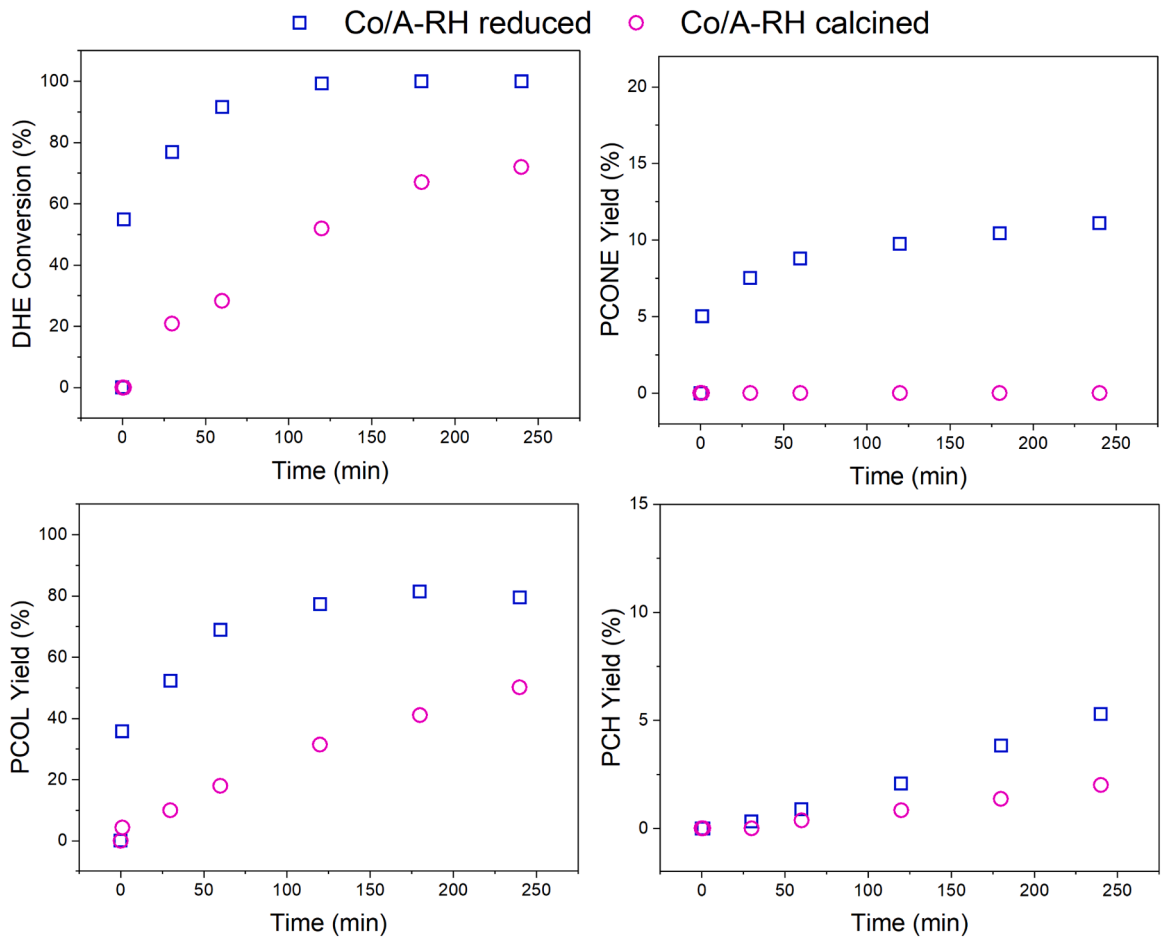

Fig. 11. Comparison of IE HDO over Co/A-RH calcined (blue dotted line) and reduced (light blue solid line). Reaction conditions: IE 2 mg/mL, dodecane 50 mL, 50 mg cat., 250 °C, 30 bar H_2, 900 rpm, 240 min.

less than 10 %, which was attributed to the high dispersion of the cobalt phase on the highly ordered mesoporous structure of SBA-15. However, when considering the process as a laboratory-scale screening step toward SAF production within an integrated biorefinery framework, the scalability and cost of the catalyst become critical parameters. In this context, biochar-based supports offer a clear economic and environmental advantage [84]. Even accounting for potential cost reductions upon scale-up, SBA-15 remains more suitable as a model mesoporous support to investigate structure–activity relationships than as an industrial catalyst material [47,48]. In contrast, biochars derived from secondary biomass such as rice husk represent a more sustainable and circular alternative, combining low cost, renewable origin, and tunable physicochemical properties suitable for large-scale applications.

3.3. *Mechanistic considerations*

To complement experimental data, the lumped reaction mechanism as shown in Fig. 1, was expanded in more detail using DFT. The reaction network was decomposed into all possible elementary steps, which are characterized by the formation or cleavage of one bond at a time. Hence, there is a need to account also for intermediates that are only stable while adsorbed and cannot be experimentally isolated (*e.g.* cyclodienes and cycloolefins). It is difficult to imagine that three hydrogen molecules are added to the aromatic ring at the same time. An alternative depicted in Fig. 12 assumes sequential addition of six H atoms. Other options in general are possible, like addition of a pair of adsorbed hydrogen or a molecularly adsorbed hydrogen. In the current study sequential addition of hydrogen atoms was only considered. Similarly, demethoxylation is usually modelled as a lumped step, but the exact mechanism among several possibilities can only be inferred from atomistic mechanistic studies. Even when it is in principle possible to distinguish between different pathways, a fast conversion can make this unfeasible. For instance, conversion of DHE to PCOL proceeds rapidly with no detectable intermediates. Hence, density functional theory (DFT) calculations were performed to analyze the conversion of IE over Co(0001) surface, chosen as representative and most stable cobalt surface [85]. Admittedly, this is a simplified model of a more complex dynamic catalyst structure.

Given the presence of four distinct active motifs - allyl, hydroxyl, methoxy groups, as well as the aromatic ring - the hydrogenation of IE to PCH can proceed through multiple pathways. Experimentally, it was shown that the allyl group is saturated first, yielding DHE. While demethoxylation always precedes dihydroxylation, it is challenged by ring hydrogenation (as postulated in Fig. 1). Two general routes are feasible: allyl hydrogenation, demethoxylation, ring hydrogenation, dehydroxylation *or* allyl hydrogenation, ring hydrogenation, demethoxylation, dehydroxylation, as depicted in Fig. 12.

The computational study, conducted without prior assumptions, evaluated the activation barriers and the reaction energy change for the possible pathways. First, the allyl double bond is saturated in two fast reaction steps with barriers of 0.58 and 0.76 eV. The ensuing DHE is most likely to be demethoxylated via the following intermediates R-OCH_3, R-OCH_2, R-OCH, R-OC, and R to yield 4-propylphenol (R = 4-propylphenoxy). The last step is fast and effectively irreversible on account of its high exothermicity, brough about by the expulsion of a stable CO molecule.

Table 7
Comparison of PCH yield obtained with different reported heterogeneous catalysts.

Entry	Carbon based catalyst	Solvent	Reaction conditions	PCH yield (%)	Ref
1	Pt/AC[a]	n-decane	2 h, 280 °C, 30 bar	25	[7]
2	PtRe/C[a]	dodecane	4 h, 300 °C, 30 bar	84	[14]
3	Ni/graphite[a]	dodecane	4 h, 300 °C, 30 bar	60	[30]
4	RuRe/MWCNT[b]	heptane	1 h, 200 °C, 30 bar	63	[18]
5	Ru/C + Nb_2O_5[c]	H_2O + MeOH	12 h, 250 °C, 11 bar	74	[81]
6	Ru/CNT[b]	H_2O + dodecane	3 h, 220 °C, 50 bar	94	[82]
7	Pd/C + HZSM−5[b]	H_2O	0.5 h, 240 °C, 20 bar	64	[83]
Entry	**Non noble metal-based catalyst**	**Solvent**	**Reaction conditions**	**PCH yield (%)**	**Ref**
8	Ni/SBA−15[a]	dodecane	4 h, 300 °C, 30 bar	75	[23]
9	Co/SBA−15[a]	dodecane	4 h, 300 °C, 30 bar	63	[30]
10	Ni/HZSM−5[b]	hexane	2 h, 250 °C, 30 bar	56	[45]
11	Ni/Al-SBA−15-HZSM−5[b]	dodecane	2 h 260 °C, 30 bar	68	[22]
12	Ni/Al-SBA−15[b]	dodecane	2 h 240 °C, 20 bar	85	[22]
13	Co/A-RH	dodecane	4 h, 300 °C, 30 bar	55	this work
14	Co/AC	dodecane	4 h, 300 °C, 30 bar	75	this work

[a] IE,
[b] EU,
[c] IE+DHE+ 4-allyl-syringol

In this pathway, the rate determining step is the cleavage of the first C-H bond in the methoxy group, which has a barrier of 0.84 eV, while all subsequent steps are much faster with barriers below 0.5 eV. Once 4-propylphenol is formed, it undergoes stepwise ring hydrogenation to form 4-PCOL. Again, the rate-determining step is first addition of a hydrogen atom, which breaks the aromaticity of the ring with a barrier of 1.15 eV and reaction energy of + 0.56 eV. Subsequent steps are faster with barriers between 0.4 and 0.8 eV. Ultimately, 4-PCOL is dehydroxylated to PCH.

Small concentrations of PCONE and other intermediates are ascribed to non-zero contributions of other pathways, shown in Fig. 12, on account of not dissimilar barriers. For instance, if DHE initially underwent ring hydrogenation instead of demethoxylation, the kinetics and energetics of hydrogenation steps would remain roughly the same. Also, demethoxylation has a notoriously complex pathway, where R-OCH and R-OCH_2 can also cleave off CH and CH_2, respectively, instead of H, only to end up with a less reactive R-O, which can still convert to 4-propylcatechol (PC).

Hydrogenation reactions are enabled by activated hydrogen atoms residing on the catalyst. On Co(0001), the adsorption energy of H* relative to ½H_2 is −0.49 eV (Gibbs free energy of −0.19 eV), which ensures highly active H*, as evidenced by the low energy barriers for hydrogenation reactions. On CoO(111), which was used as a model for Co^{2+} species, the adsorption energy of H* is −2.67 eV on O and −1.10 eV on Co^{2+}, which is prohibitively strong to allow efficient hydrogenation of hydrocarbons. Thus, Co^{2+} allows for facile H_2 dissociation, while the ensuing H* then spills over to Co(0), where it can hydrogenate eugenol and other intermediates.

3.4. Kinetic study

In terms of reaction kinetics, only a few studies reported the initial rate for DHE conversion, with values of 0.30 and 6.17 mmol/min g_{metal} for Ni-SBA-15 [23] and PtRe/C [14], respectively. The initial rate observed for all the catalysts tested falls within the range (0.68–1.68 mmol/min g_{metal}, Table 6), indicating competitive activity. However, in the case of Co/A-RH, the disappearance of DHE was too fast to determine the initial rate, showing a remarkable activity of this catalyst. Therefore, Co/A-RH was chosen to investigate the reaction at different conditions, to get better insights into its performance, reaction network and activation energy of each step. In particular, the effect of temperature, H_2 pressure, catalyst amount and IE concentration were evaluated, with the results listed in Table 8.

Remarkably, the use of biochar as a support for cobalt-based catalysts offers several potential advantages, including lower costs, simplified preparation procedures, and a reduced environmental impact. Biochar, being a sustainable and low-cost material derived from biomass, provides an eco-friendly alternative to synthetic carbon supports, aligning with the goals of green chemistry and sustainable catalysis.

3.4.1. Effect of temperature

The effect of temperature was clearly visible in the initial rate for formation of PCH, as it increased with increasing temperature. As detailed in Table 8 (entries 1–4) and illustrated in Fig. 13, increasing the reaction temperature from 200 °C to 300 °C at a constant pressure of 30 bar resulted in an enhanced reaction rate.

The product distribution was notably temperature dependent. For clarity, the yields of the main products obtained at different temperatures (200–300 °C, 30 bar H_2, 240 min) are reported in Fig. S7 as bar plots, providing a clearer visual comparison of the effect of temperature on selectivity). At 200 °C, the predominant product was PCOL with a yield of 84 %, while only 0.5 % of PCH was produced. As the temperature increased, the cleavage of the hydroxyl group's carbon-oxygen bond became more favorable, leading to a PCH yield of 55 % at 300 °C. This shift can be attributed to different temperature dependencies of the hydrogenation and deoxygenation steps; hydrogenation, characterized by a lower activation energy, was favored at lower temperatures, whereas deoxygenation, which has a higher activation energy, became more favorable at elevated temperatures [11]. From the Arrhenius plot of the initial rates of PCH reported in Fig. 14, the activation energy was calculated as 182.9 kJ/mol. Notably, at 275 °C 45.0 % yield of PCH, and 44.7 % yield of PCOL were obtained, corresponding to a carbon balance of 95.6 %. Consequently, 275 °C was selected as the optimal temperature for further investigations to minimize side reactions.

3.4.2. Effect of pressure

The effect of H_2 pressure (between 10 and 40 bar) was investigated, both at low temperature (200 °C) (Fig. 15, Table 8, entries 1, 5, 6) and at high temperature (275 °C) (Fig. 16 and Table 8, entries 3, 7, 8). In both cases, the increasing of H_2 pressure had a positive effect on the reaction rate. Higher pressure increases the solubility of hydrogen in the reaction medium, and diffusion of hydrogen to the active sites, promoting hydrogenation steps. At 200 °C, the reaction occurred selectively only towards the formation of PCOL, and the final yield rose from 55.0 % to 96.5 % as the pressure increased from 20 to 40 bar. These results are in line with the study of Liu et al. [86] who investigated different Co based catalysts (TiO_2, HZM-5, ZrO_2, CeO_2, SiO_2) in selective HDO of phenols to cyclohexanols at relatively mild conditions. At 275 °C the C-O cleavage of the PCOL hydroxy group was favored, and the initial PCH formation rate increased as follows: 0.03 mmol/min/g_{Co} at 10 bar, followed by 0.08 mmol/min/g_{Co} at 20 bar and 0.18 mmol/min/g_{Co} at 30 bar, respectively (Fig. 17). Interesting to note that the apparent reaction order in hydrogen clearly exceeds unity, as visible from Fig. 17.

The influence of pressure was less remarkable at a higher

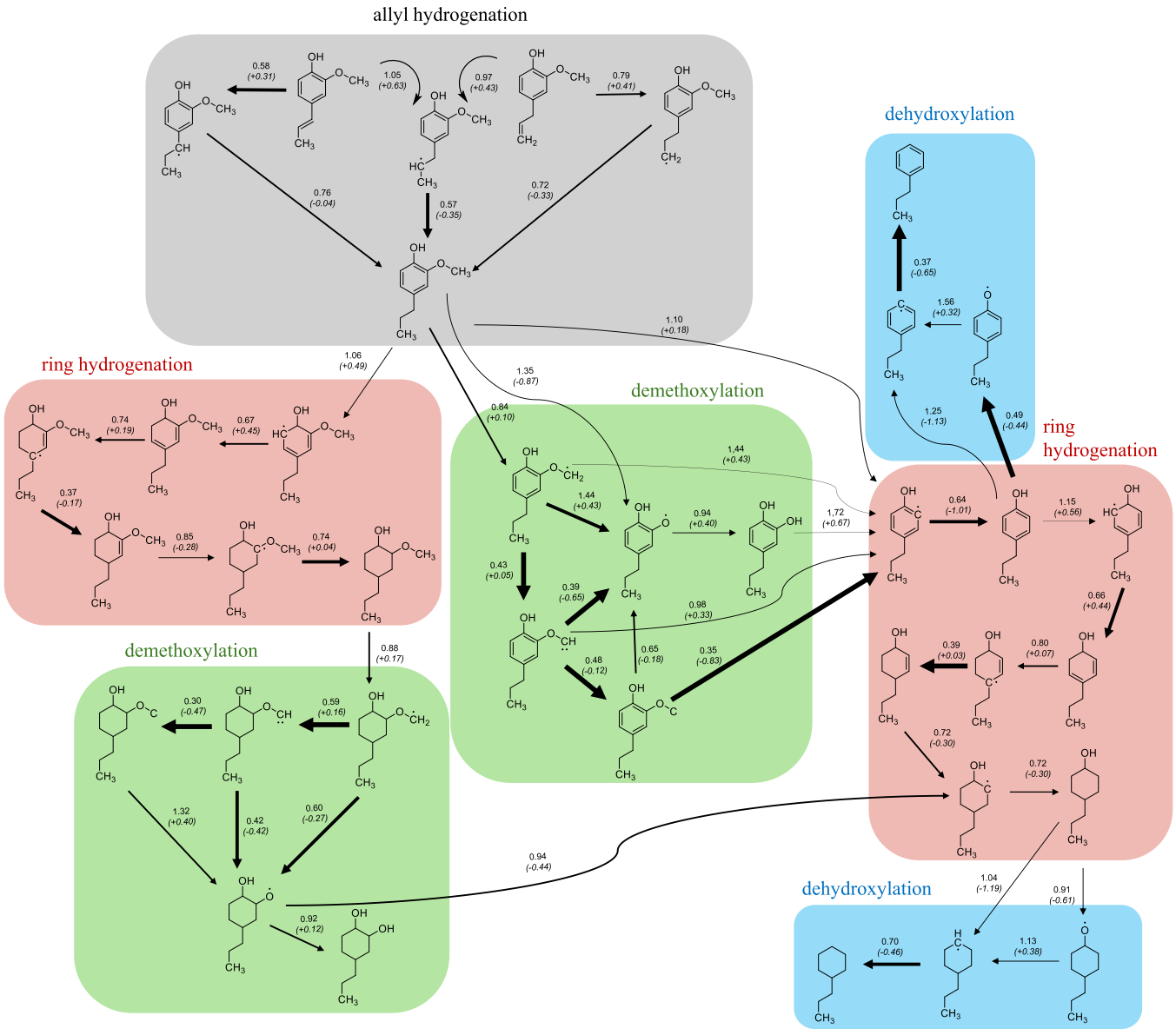

Fig. 12. Reaction network including all possible elementary reactions for hydrodeoxygenation of IE to PCH. Barriers (E_A) reported in bold (in eV), reaction energies (ΔE) given in parentheses (in eV). The width of the arrows linking intermediates is proportional to exp(-E_A) of each step. Note that a thick arrow corresponds to a fast conversion of an intermediate *if* it is formed in the previous steps.

temperature, however, the PCH yield at 90 % DHE conversion increased from zero at 10 bar and 20 bar to 37 % at 30 bar indicating that the consecutive reactions are slow under low hydrogen pressures. The final yields of PCH increased from 16.8 % < 25.6 % < 45 % when applying 10, 20 or 30 bar total pressure. The increase of pressure had also a positive effect on the carbon balance, both at 200 °C and 275 °C, suggesting that a high H_2 pressure suppressed side reactions. This effect is more pronounced at low temperature, where the reaction rate for HDO is lower and therefore side reactions are more likely to occur. This result is in line with Alda-Onggar et al. [15] reporting that the liquid phase mass balance closure was also the highest in HDO of isoeugenol using Ir-Re/Al_2O_3 catalyst under the highest applied pressure, 40 bar.

3.4.3. *Effect of IE concentration*

The effect of the initial reactant concentration was investigated by increasing the IE concentration from 2 mg/mL to 6.5 mg/mL, using 50 mg Co/A-RH, at 275 °C and 30 bar H_2, in 50 mL of dodecane. (Table 8, entries 3, 9, 10). The experimental data for the initial rate of PCH formation as a function of IE concentration were best described by Eq. 6 and Fig. 18, consistent with the Eley-Rideal type kinetics, suggesting that the reaction involves the adsorption of one reactant (IE) on the catalyst surface.

$$r_0 = \frac{kCP_{H2}}{1+KC} = \frac{k1C}{1+KC} \qquad (6\quad ,\quad)$$

At low IE concentrations, the rate increases almost linearly with concentration, while at higher concentrations, the rate tends to an eventual plateau due to the saturation of active sites. The adsorption constant (K ≈0.47 mL/mg) indicates a moderate affinity of IE for the catalyst surface, balancing efficient surface interaction with limited site saturation.

3.4.4. *Kinetic modelling*

Considering the experimental observations and the results from DFT calculations, the reaction can be simplified to a reaction network shown in Fig. 19 and consisting of six reaction routes, which implicitly include

Table 8
Results from HDO of isoeugenol using Co/A-RH catalyst under different conditions.

Entry	T (°C)	P (bar)	[IE] mg/mL	Cat. (mg)	Initial rate for PCH formation (mmol/min g_{Co})	DHE Conversion[a] (%)	PCONE Yield[b,c] (%)	PCOL Yield[b,c] (%)	PCH Yield[b,c] (%)	C balance (%)
1	200	30	2	50	-	100	0	79 (84)	0 (0.5)	84.5
2	250	30	2	50	0.01	100	8 (11)	67 (79.4)	1 (5.3)	95.8
3	275	30	2	50	0.18	100	0 (5.9)	73 (44.7)	37 (45.0)	95.6
4	300	30	2	50	0.38	100	n.a. (0.7)	n.a. (1.7)	n.a. (55.1)	57.5
5	200	20	2	50	-	79.4	n.a. (0)	n.a. (55.5)	n.a. (0)	75.8
6	200	40	2	50	-	100	0	83 (96.5)	0	96.5
7	275	10	2	50	0.03	100	13 (6.5)	60 (65.7)	0 (16.8)	88.9
8	275	20	2	50	0.08	100	12 (9.1)	69 (55.8)	0 (25.6)	90.5
9	275	30	3.5	50	0.23	100	10 (8.3)	90 (59.4)	3 (27.4)	95.2
10	275	30	6.5	50	0.28	100	3 (5.2)	65 (62.2)	1 (20.5)	87.8
11	275	30	2	20	0.04	100	8 (5.6)	68 (72.7)	3 (14.5)	92.9
12	275	30	2	80	0.33	100	n.a. (1.5)	n.a. (24.7)	n.a. (65.2)	91.0
13	275 (II)	30	2	50	0.17	100	4.5	43.2	42.7	90.5
14	275 (III)	30	2	50	0.17	100	8.4	58.6	34.6	99.0

[a] after 240 min,
[b] at DHE conversion level of 90 %,
[c] in parenthesis after 240 min.

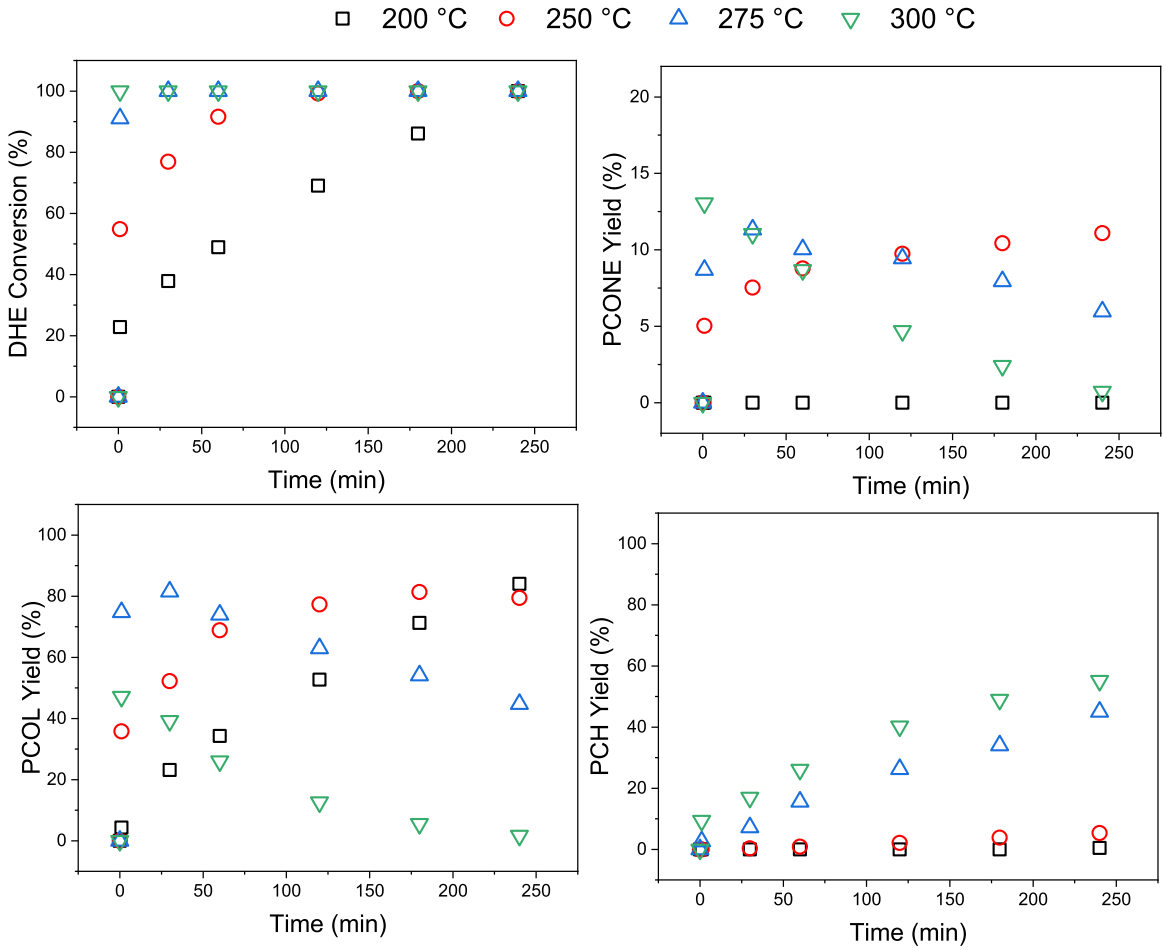

Fig. 13. IE HDO over Co/A-RH at different reaction temperatures. Reaction conditions: 50 mg Co/A-RH (< 63 μm), IE 2 mg/mL, dodecane 50 mL, 30 bar H_2, 900 rpm, $_2$40 min.

addition of dihydrogen:

IE → DHE (Lumped step 1)

DHE → 4-PPHOL (Lumped step 2)

4-PPHOL → PCONE (Lumped step 3)

4-PPHOL → PCOL (Lumped step 4)

PCONE → PCOL (Lumped step 5)

PCOL → PCH (Lumped step 6)

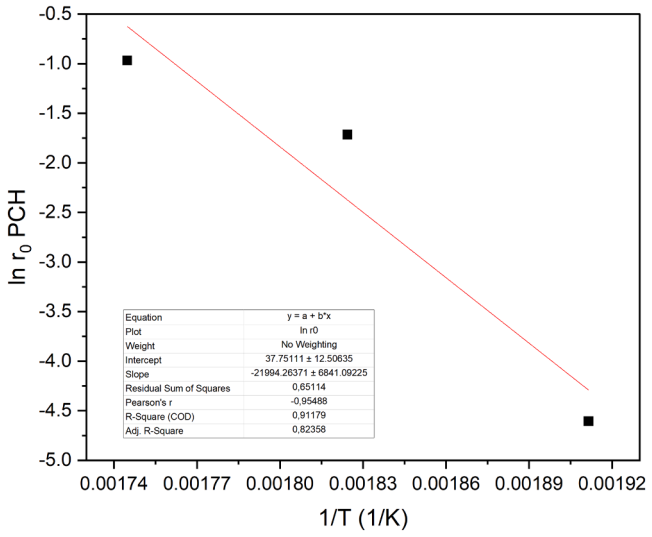

Fig. 14. Arrhenius plot for PCH formation.

For initial estimates for their apparent activation energies, the ab initio barriers for the first elementary step of each lumped step can be used, since subsequent elementary steps are faster.

The reaction network takes into account a direct route in which 4-PPHOL is hydrogenated to PCONE, and a parallel reaction route where 4-PPHOL reacts directly to PCH via PCOL. Moreover, it is also considered the transformation of IE to unknown compounds (U), to close the carbon balance.

The following rate equations were proposed (Eqs. 7–14):

$$r_1 = k_1 * c_{IE} * p_{H2} / D \quad (7)$$

$$r_2 = k_2 * c_{DHE} * p_{H2} / D \quad (8)$$

$$r_3 = k_3 * c_{4\text{-PPHOL}} * (p_{H2})^2 / D \quad (9)$$

$$r_4 = k_4 * c_{4\text{-PPHOL}} * p_{H2} / D \quad (10)$$

$$r_5 = k_5 * c_{PCONE} * p_{H2} / D \quad (11)$$

$$r_6 = k_6 * c_{PCOL} * p_{H2} / D \quad (12)$$

$$r_7 = k_7 * c_{IE} * p_{H2} / D \quad (13)$$

$$\text{and } D = 1 + \sum K_i C_i \quad (14)$$

where K_i is the adsorption equilibrium constant and C_i is the concentration of the compound i. Preliminary data fitting indicated that D≈ 1. In Eqs. (7), (8) and (10)-(13) the reaction order in hydrogen was sent to be equal to unity for simplification. For Eq. (9) the reaction order exceeding unity was also tested giving the value close to 2, which was then fixed.

The mass balances for each compound are given as (Eqs. 15–21):

$$Dc_{IE}/dt = -(r_1 + r_7) * \rho_B \quad (15)$$

$$Dc_{DHE}/dt = (r_1 - r_2) * \rho_B \quad (16)$$

$$Dc_{4\text{-PPHOL}}/dt = (r_2 - r_3 - r_4) * \rho_B \quad (17)$$

$$Dc_{PCONE}/dt = (r_3 - r_5) * \rho_B \quad (18)$$

$$Dc_{PCOL}/dt = (r_4 + r_5 - r_6) * \rho_B \quad (19)$$

$$Dc_{PCH}/dt = (r_6) * \rho_B \quad (20)$$

$$Dc_{Unknown}/dt = r_7 * \rho_B \quad (21)$$

where $\rho_B$is the catalyst bulk density ($\frac{m_{cat}}{V_{liquid}}$).

Kinetic modelling was performed using MODEST software [87] by solving the differential equations with the backward difference method. For the parameter estimation the simplex and the Levenberg-Marquardt methods were applied. The objective function θ and the degree of explanations were defined as (22-23):

$$\theta = \sum^{n} (y_i - \hat{y}_i)^2 \quad (22)$$

$$R^2 = 1 - \frac{(y_i - \hat{y}_i)^2}{(y_i - \bar{y}_i)^2} \quad (23)$$

In which $\hat{y}_i$ denotes the estimated value and $\bar{y}_i$ the mean value of observations. The model fits are shown in Fig. 20 and Fig. S8, the parameter values are given in Table 9, and the correlation matrix of the parameters is reported in Table S3. Overall, the model explains the experimental data with a high degree of accuracy (93.14 %). In many cases, the model closely follows the experimental trends, indicating that the kinetic parameters and reaction pathways chosen are appropriate for most conditions. However, a notable deviation is observed at 200 °C under 40 bar (Fig. S8).

Despite the uncertainty associated with some parameters, the obtained kinetic constants allow drawing meaningful correlations with the experimental data. Specifically, the calculated value of k_1, corresponding to the hydrogenation of IE to DHE, is extremely high, in agreement with the experimental evidence that the saturation of the C=C bond

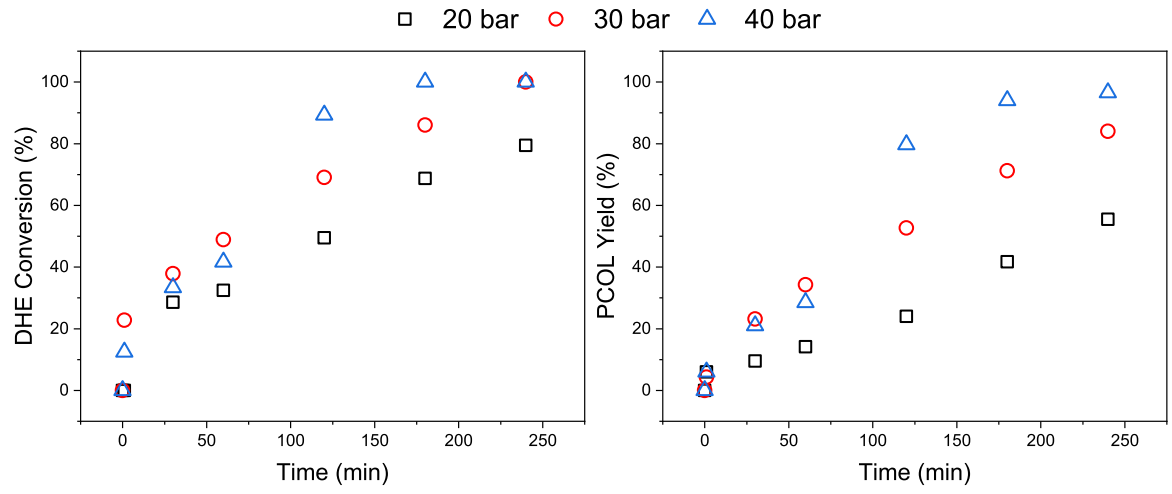

Fig. 15. IE HDO at different pressures, low temperature. Reaction conditions: 50 mg Co/A-RH (< 63 μm), IE 2 mg/mL, dodecane 50 mL, 200 °C, 900 rpm, 240 min.

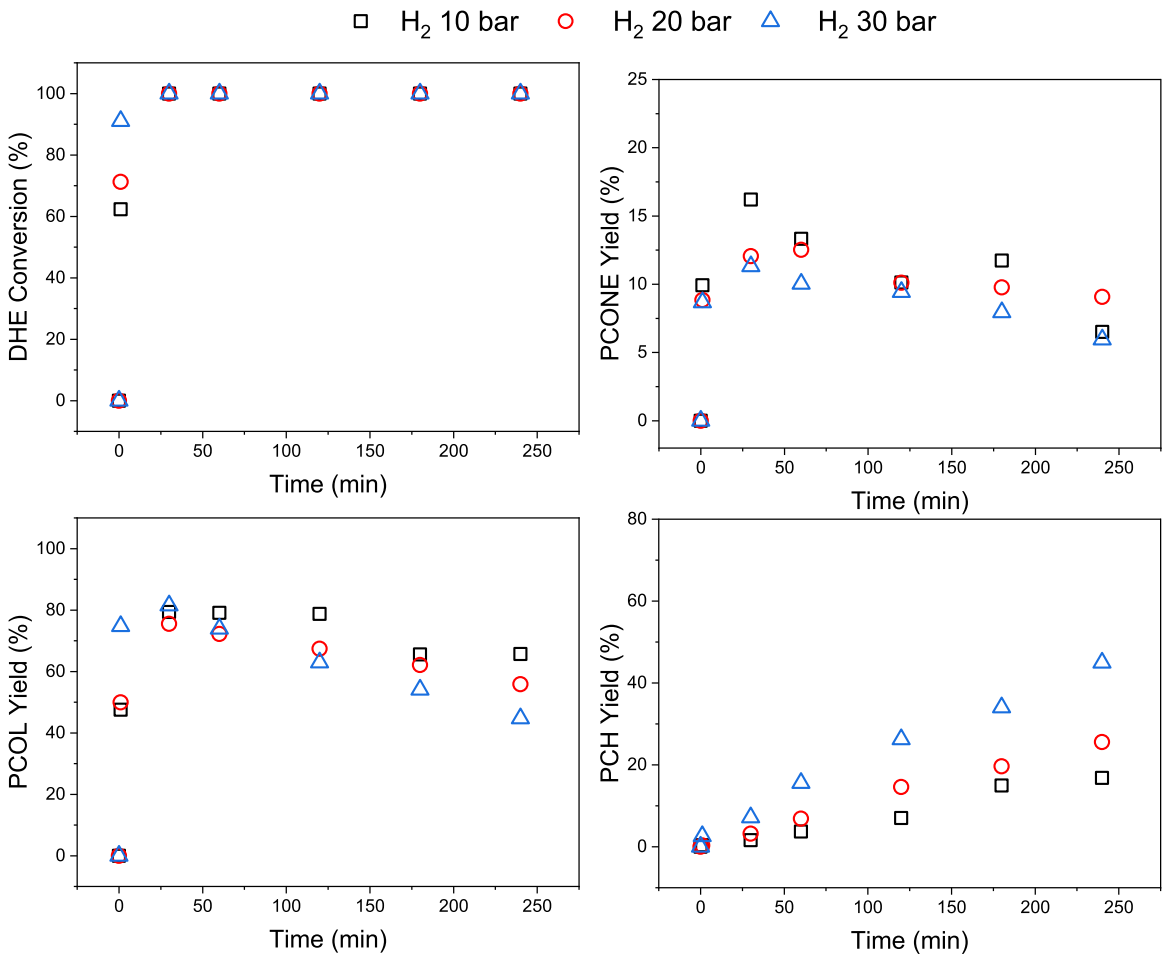

Fig. 16. IE HDO at different pressures, high temperature. Reaction conditions: 50 mg Co/A-RH (< 63 μm), IE 2 mg/mL, dodecane 50 mL, 275 °C, 900 rpm, 240 min.

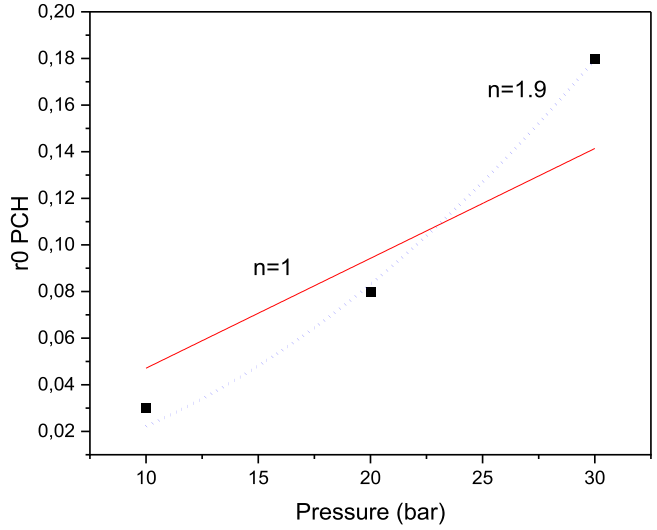

Fig. 17. Initial reaction rate for PCH formation vs. pressure at 275 °C.

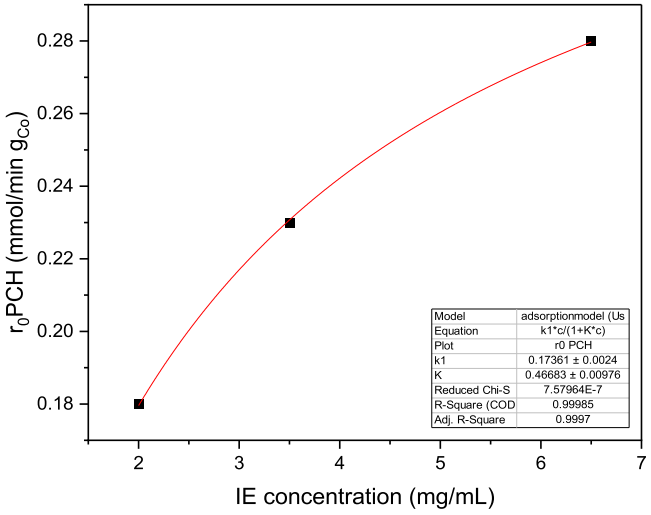

Fig. 18. IE HDO at different IE concentrations. Reaction conditions: 50 mg Co/A-RH (< 63 μm), dodecane 50 mL, 275 °C, 30 bar H_2 900 rpm, ₂40 min. Fitting of the data to Eq. (6).

proceeds rapidly, even in the absence of a catalyst [88]. Conversely, the values of k_2 and k_3 are much lower, however, comparable to each other, thereby indicating similar rates of formation and consumption of the intermediate 4-PPHOL. This could explain why this compound is not detected during the experiments. Furthermore, the comparison between k_3 and k_4 suggests that the transformation of 4-PPHOL to PCOL (k_4) is kinetically favored over the pathway leading to PCONE (k_3), consistent with the experimentally observed formation of PCONE in only minor amounts and its absence at a lower temperature (200 °C). The small value of k_5 also supports this interpretation, confirming that the route

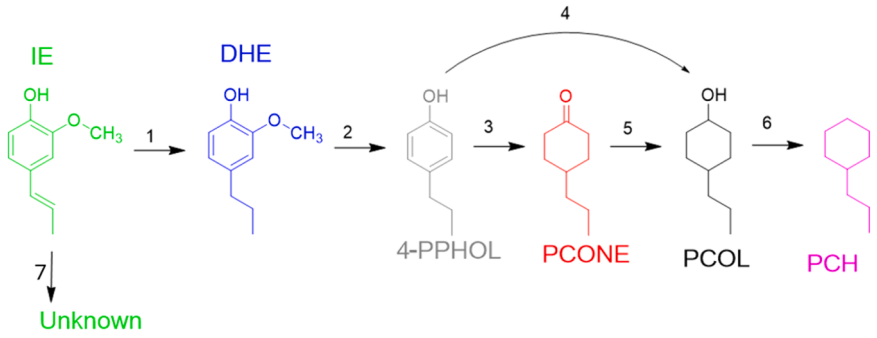

Fig. 19. Proposed lumped reaction network for HDO of Isoeugenol.

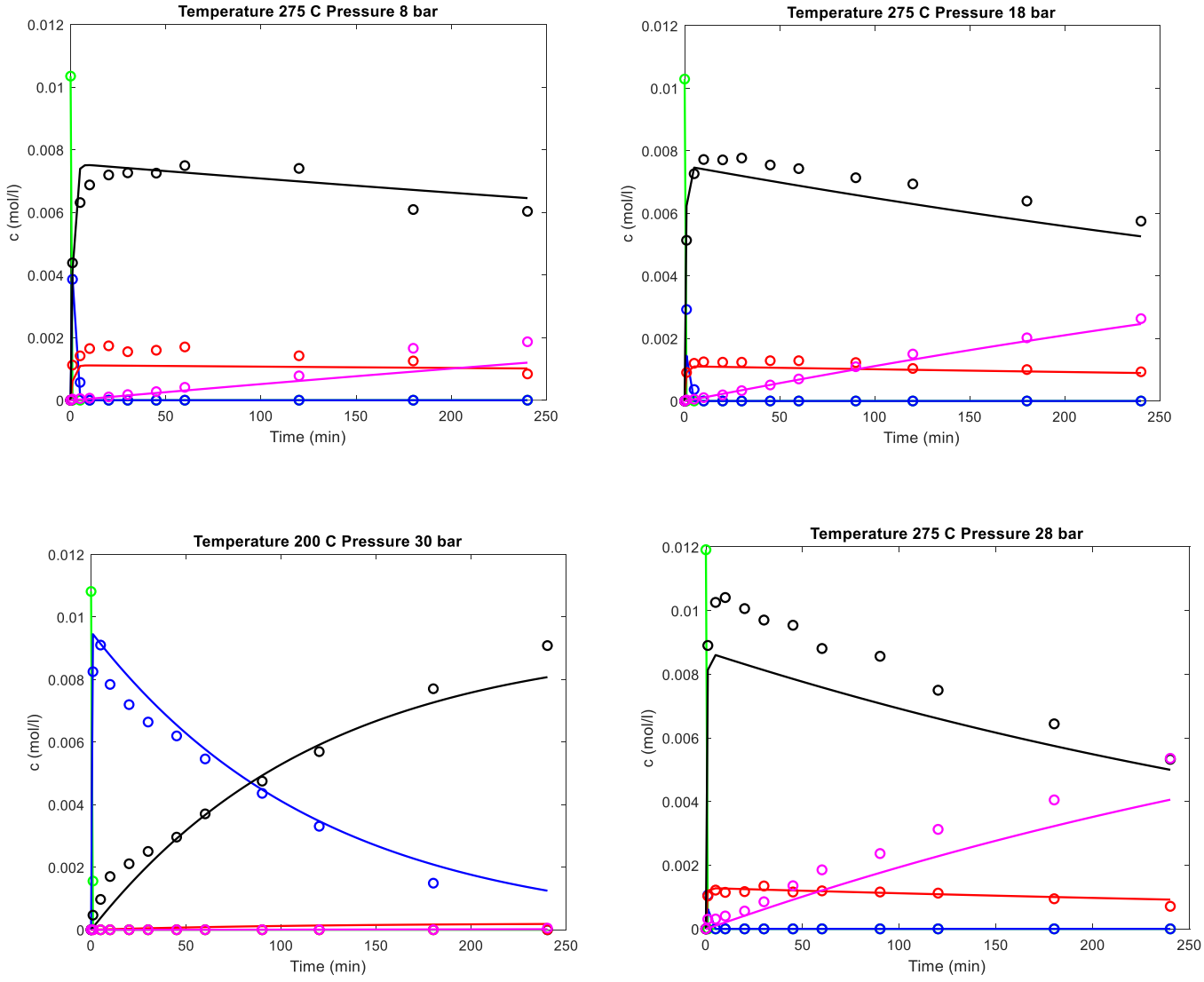

Fig. 20. Experimental kinetic results and model fit for IE transformation at different reaction conditions. IE (green), DHE (blue). PCOL (black), PCONE (red), PCH (pink).

through PCOL is predominant. Finally, the low value of k_6 indicates that the hydrogenolysis of the hydroxyl group, which leads to the final product PCH, is the rate determining step of the overall network.

Not many examples of kinetic modeling for this reaction are reported in the literature; therefore, our results were compared with those obtained by Tieuli et al. using Ni/SBA-15 as a catalyst [23]. The calculated kinetic constants and activation energies are comparable in the order of magnitude. However, Tieuli et al. described formation of propylcyclohexane (PCH) through an intermediate propylcyclohexene species, which was not detected under our experimental conditions. Consequently, a direct quantitative comparison between the two models is not straightforward, although both studies consistently identify the hydrogenolysis step leading to PCH as kinetically demanding.

From the kinetic modeling, the activation energy for the formation of

Table 9
The results from kinetic modelling.

Parameter	Estimated	Standard error (%)
k_1	69.9	15.7
k_2	0.09	8.9
k_3	0.09	11.5
k_4	19.0	16.7
k_5	$0.48 \cdot 10^{-4}$	54.0
k_6	$0.81 \cdot 10^{-4}$	6.4
k_7	16.1	15.4
	kJ/mol	
E_{A1}	57.0	> 100
E_{A2}	170	1.6
E_{A3}	84.1	50.7
E_{A4}	30.4	> 100
E_{A5}	87.8	86.2
E_{A6}	151	6.3
E_{A7}	70.5	> 100

PCH resulted 151 kJ/mol, with a small error, indicating good parameter confidence. This value is lower than the apparent activation energy calculated by the Arrhenius plot from the experimental values (182.9 kJ/mol, Fig. 14). This difference may stem from the inherent simplifications of the Arrhenius approach, which does not account for potential variations in reaction order, catalyst deactivation, or intermediate equilibria. The lower activation energy from the model could also reflect the influence of a rate-limiting step that becomes dominant under specific conditions and is better resolved through detailed kinetic modeling than from a simple global fit.

3.5. Catalyst recyclability

The stability and recyclability of Co/A-RH were evaluated over three consecutive reaction cycles at 275 °C and 30 bar. Among the cycles, the catalyst has been thoroughly washed with acetone, dried and then reduced at the same conditions as for the first cycle. Solvent extraction of the organic deposits was chosen despite of calcination to avoid combustion of the support or substantial modifications to the carbonaceous structure due to oxidative treatment [89].

As depicted in Fig. 21, the catalyst exhibited good stability in the first 2 cycles, maintaining consistent activity. A slight decline in performance was observed in the third cycle, with approximately a 10 % decrease in the final yield of PCH, denoting a partial deactivation occurring during the third cycle. However, it is noteworthy that the initial reaction rates for PCH formation remained almost unchanged across all three cycles (Table 8), suggesting that the active sites were still accessible at the beginning of each reaction and that deactivation primarily affected the later stages of the process. TEM microscopy and ICP analyses of the spent catalyst demonstrated that no leaching or sintering of the Co nanoparticles occurred (Fig. 22, Table 9). Although the nanoparticles showed a slightly broader size distribution compared to the fresh catalyst (Fig. 22), the average diameter was smaller (7.7 ± 0.3 nm vs 8.9 ± 0.2 nm, Table 9).

This reduction in size could be attributed to the partial reduction of Co in the reaction environment, leading to shrinkage of the nanoparticles due to the loss of the external oxide layer. XPS analyses confirmed this, showing a higher contribution from the Co° signal in the spent Co/A-RH catalyst (ca. 11 % vs 5 %) (Table 10) [28]. The slight decrease in activity can be therefore correlated with an increase of the

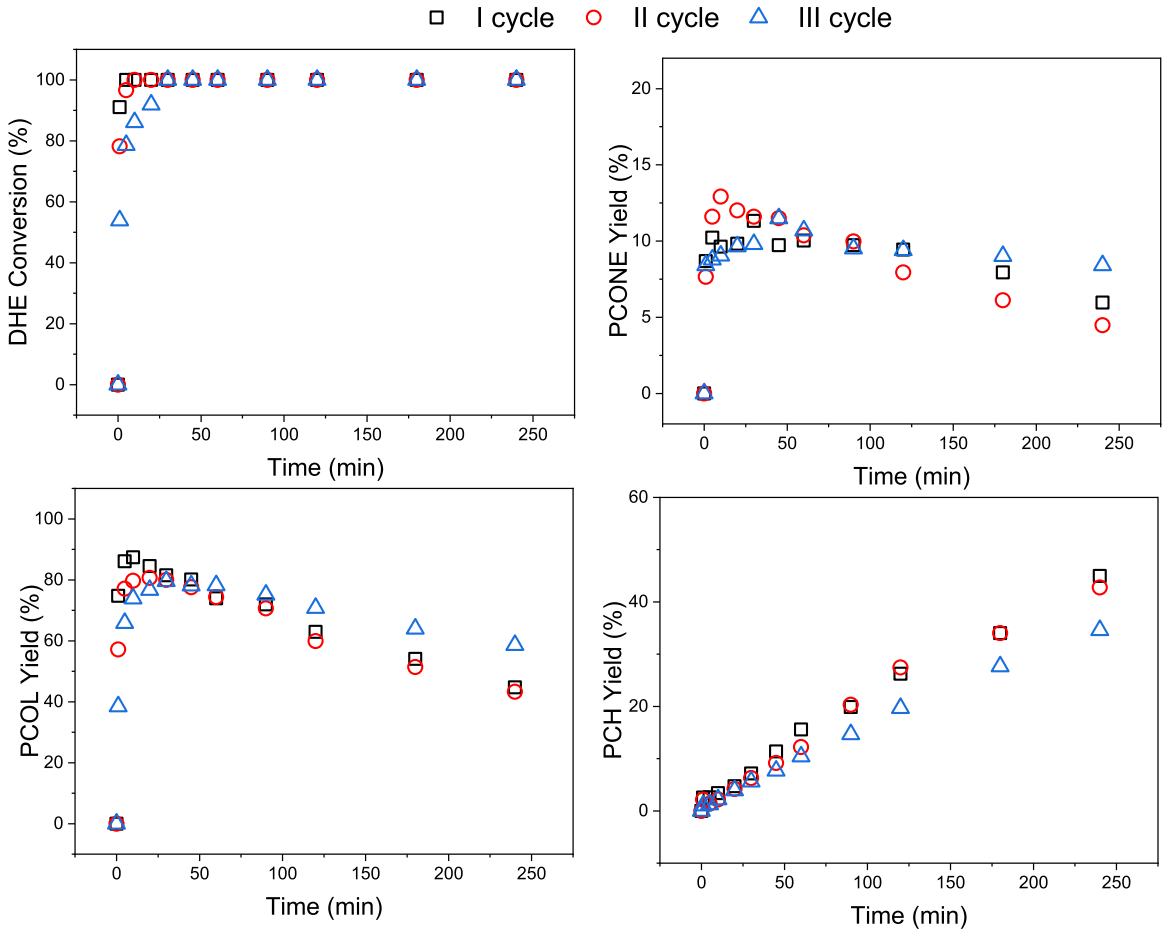

Fig. 21. Catalyst recyclability. Reaction conditions: 50 mg Co/A-RH (< 63 μm), dodecane 50 mL, IE 2 mg/mL, 275 °C, 30 bar H_2 900 rpm, $_2$40 min.

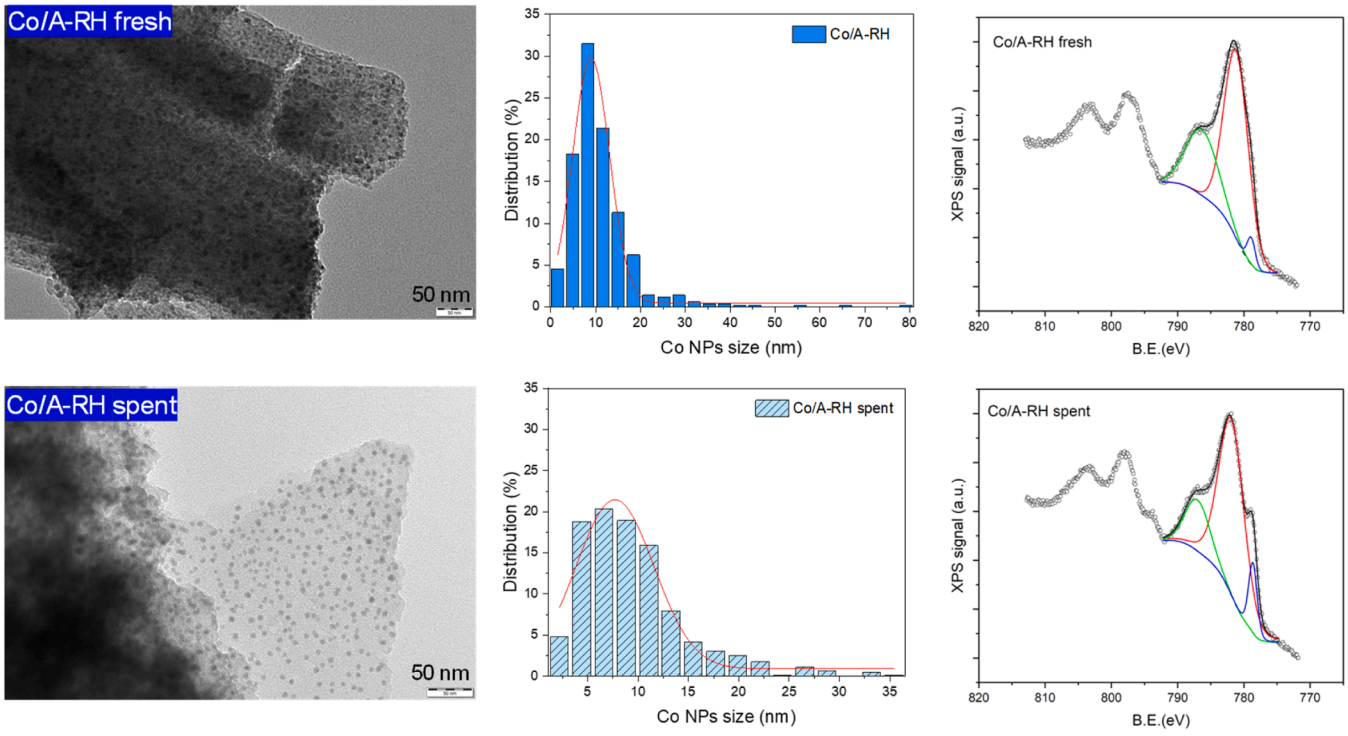

Fig. 22. TEM microscopy, Co NPs size distribution, and Co2p XPS spectra of Co/A-RH fresh, and Co/A-RH spent, after 3 reaction cycles.

Table 10
Characterizations of the fresh and spent Co/A-RH catalyst: CHNS, ICP, TEM and XPS.

Sample	C (%)	H (%)	N (%)	S (%)	Co wt %	D_{TEM} (nm)	Co 2p (eV) (atomic %)	
							Co^0	Co^{2+}
Co/A-RH fresh	31.99	0.98	0.39	0.06	12	8.9 ± 0.2	778.9 (4.6)	781.2 (95.4)
Co/A-RH spent	34.99	0.95	0.39	0.06	12	7.7 ± 0.3	778.6 (11.4)	781.9 (88.6)

metallic cobalt phase, as also reported by Shetty et al., who confirmed the crucial role of Co^{2+} in the hydrogenolysis processes [90]. Moreover, CHNS analyses (Table 10) revealed a slight increase in carbon content on the spent catalyst, suggesting that even after washing, a small residue of heavier organic compounds remained on the material, probably in the form of coke. These organic deposits, along with the partial reduction of the metal phase, contributed to minor deactivation of Co/A-RH after three reaction cycles. However, the absence of leaching and sintering is a highly positive outcome for this biochar-based catalyst, highlighting its potential stability in the repeated use. Further optimization of reduction conditions and surface cleaning strategies could help mitigate deactivation, enhancing the catalyst longevity and performance.

4. Conclusions

In this work, for the first time the use of cobalt on biochar-based catalysts was investigated for hydrodeoxygenation of isoeugenol, as a bio-oil model compound. Among the tested catalysts, Co/A-RH derived from rice husk demonstrated the best performance, achieving full conversion IE within a few minutes, achieving 55 % yield of propylcyclohexane after 240 min at 300°C and 30 bar H_2. A decrease in the reaction temperature by only 25 °C drastically improved the carbon balance from 57.5 % to 96.5 %, suppressing side reactions. Also Co/AC, supported on a commercial active carbon demonstrate high activity, reaching 75 % of PCH yield at the same conditions. The superior performance of these two catalysts was attributed to the good metal dispersion and the interaction with the support, resulting in a partial reduction which led to the coexistence of Co^0 and Co^{2+} species. The synergy between these sites enabled efficient hydrogenation and C–O bond cleavage while maintaining stability during recycling, with no evidence of metal leaching or sintering. A slight decrease in activity after reuse was attributed to increased ratio of Co^0 phase, and surface coverage by reaction residues.

Considering the impact of various reaction parameters (temperature, pressure, IE concentration), a detailed reaction network was proposed and explored using the DFT calculations, allowing the calculation of the rate constants and the activation energies for each reaction route. These results demonstrate the potential of biochar-derived supports for designing efficient and stable catalysts for hydrodeoxygenation reactions.

CRediT authorship contribution statement

Kari Eränen: Supervision, Methodology. **Mika Lastusaari:** Validation, Supervision. **Murzin Dmitry Yu:** Writing – review & editing, Validation, Supervision, Resources, Project administration, Conceptualization. **Michela Signoretto:** Writing – review & editing, Validation, Supervision, Project administration, Funding acquisition. **Davide Baldassin:** Methodology, Investigation. **Päivi Mäki-Arvela:** Writing – review & editing, Validation, Supervision, Methodology, Data curation. **Johan Wärnå:** Formal analysis, Data curation. **Anssi Peuronen:** Formal analysis. **Matej Huš:** Writing – original draft, Formal analysis, Data curation. **Blaž Likozar:** Validation, Data curation. **Atte Aho:** Formal analysis, Data curation. **Mark E. Martinez Klimov:** Supervision, Methodology, Formal analysis. **Olha Yevdokimova:** Formal analysis. **Lilia Longo:** Writing – original draft, Methodology, Investigation.

Declaration of Competing Interest

The authors declare that they have no known competing financial interests or personal relationships that could have appeared to influence

the work reported in this paper.

Acknowledgements

The financial support from the Slovenian Research and Innovation Agency through core funding (P2–0152), infrastructure funding (I0–0039), travel fund (BI-FIN/25–27–011) and project funding (J7–4638, N2–0316) is greatly appreciated. The research was (co-)funded under the HyBReED project, supported by the European Union – NextGenerationEU. The authors acknowledge the HPC RIVR consortium and EuroHPC JU for providing computing resources of the HPC system Vega at the Institute of Information Science, Maribor, Slovenia. Electron microscopy samples were processed and analyzed at the Electron Microscopy Laboratory, Institute of Biomedicine, University of Turku, which received financial support from Biocenter Finland. Materials research infrastructure/Department of Physics and Astronomy, University of Turku is gratefully acknowledged for a possibility to use their XPS. The MIUR (Italian ministry for education, university and research) is gratefully acknowledged for the financial support (doctoral scholarships) of the inter-university Ph.D. program of University of Trieste and University Ca' Foscari Venice. Conceria Pasubio S.p.A and Riseria delle Abbadesse are acknowledged for providing leather and rice husk waste.

Appendix A. Supporting information

Supplementary data associated with this article can be found in the online version at doi:10.1016/j.apcatb.2025.126194.

Data availability

Data will be made available on request.

References

[1] S. Chu, A. Majumdar, Opportunities and challenges for a sustainable energy future, Nature 488 (2012) 294–303, https://doi.org/10.1038/nature11475.
[2] B.P. Sandaka, J. Kumar, Alternative vehicular fuels for environmental decarbonization: a critical review of challenges in using electricity, hydrogen, and biofuels as a sustainable vehicular fuel, Chem. Eng. J. Adv. 14 (2023) 100442, https://doi.org/10.1016/j.ceja.2022.100442.
[3] E. Cabrera, J.M.M. de Sousa, Use of sustainable fuels in aviation—a review, Energies 15 (2022) 2440, https://doi.org/10.3390/en15072440.
[4] P. Su-ungkavatin, L. Tiruta-Barna, L. Hamelin, Biofuels, electrofuels, electric or hydrogen?: a review of current and emerging sustainable aviation systems, Prog. Energy Combust. Sci. 96 (2023) 101073, https://doi.org/10.1016/j.pecs.2023.101073.
[5] A. Androniceanu, O.M. Sabie, Overview of green energy as a real strategic option for sustainable development, Energies 15 (2022) 8573, https://doi.org/10.3390/en15228573.
[6] A. Demirbas, G. Arin, An overview of biomass pyrolysis, Energy Sources 24 (2002) 471–482, https://doi.org/10.1080/00908310252889979.
[7] V.S. Prabhudesai, R. Vinu, Hydrodeoxygenation of biomass-derived oxygenate mixtures over Pt/C and HZSM-5 mixed catalysts, Top. Catal. 66 (2023) 405–419, https://doi.org/10.1007/s11244-023-01782-y.
[8] V.S. Prabhudesai, L. Gurrala, R. Vinu, Catalytic hydrodeoxygenation of lignin-derived oxygenates: catalysis, mechanism, and effect of process conditions, Energy Fuels 36 (2022) 1155–1188, https://doi.org/10.1021/acs.energyfuels.1c02640.
[9] A. Carrasco Díaz, L. Abdelouahed, N. Brodu, V. Montes-Jiménez, B. Taouk, Upgrading of pyrolysis bio-oil by catalytic hydrodeoxygenation, a review focused on catalysts, model molecules, deactivation, and reaction routes, Molecules 29 (2024) 4325, https://doi.org/10.3390/molecules29184325.
[10] G.J.S. Dawes, E.L. Scott, J.L. Nôtre, J.P.M. Sanders, J.H. Bitter, Deoxygenation of biobased molecules by decarboxylation and decarbonylation – a review on the role of heterogeneous, homogeneous and bio-catalysis, Green. Chem. 17 (2015) 3231–3250, https://doi.org/10.1039/C5GC00023H.
[11] A. Bjelić, M. Grilc, B. Likozar, Bifunctional metallic-acidic mechanisms of hydrodeoxygenation of eugenol as lignin model compound over supported Cu, Ni, Pd, Pt, Rh and Ru catalyst materials, Chem. Eng. J. 394 (2020) 124914, https://doi.org/10.1016/j.cej.2020.124914.
[12] I. Simakova, O. Simakova, P. Mäki-Arvela, A. Simakov, M. Estrada, D.Yu Murzin, Deoxygenation of palmitic and stearic acid over supported Pd catalysts: effect of metal dispersion, Appl. Catal. A Gen. 355 (2009) 100–108, https://doi.org/10.1016/j.apcata.2008.12.001.
[13] C.A. Teles, P.M. de Souza, R.C. Rabelo-Neto, A. Teran, G. Jacobs, C. Vilela Weikert, Z.M. Magriotis, V.O.O. Gonçalves, D.E. Resasco, F.B. Noronha, Reaction pathways for the HDO of guaiacol over supported Pd catalysts: effect of support type in the deoxygenation of hydroxyl and methoxy groups, Mol. Catal. 523 (2022) 111491, https://doi.org/10.1016/j.mcat.2021.111491.
[14] M. Martinez-Klimov, P. Mäki-Arvela, A. Çiftçi, N. Kumar, K. Eränen, M. Peurla, E.J. M. Hensen, D.Yu Murzin, Bifunctional Pt–Re catalysts in hydrodeoxygenation of isoeugenol as a model compound for renewable jet fuel production, ACS Eng. Au 2 (2022) 436–449, https://doi.org/10.1021/acsengineeringau.2c00015.
[15] M. Alda-Onggar, P. Mäki-Arvela, K. Eränen, A. Aho, J. Hemming, P. Paturi, M. Peurla, M. Lindblad, I.L. Simakova, D.Yu Murzin, Hydrodeoxygenation of isoeugenol over alumina-supported Ir, Pt, and Re catalysts, ACS Sustain. Chem. Eng. 6 (2018) 16205–16218, https://doi.org/10.1021/acssuschemeng.8b03035.
[16] Z. Yu, W. Kong, Y. Guo, W. Liang, J. Liang, M. Chen, D. Zhao, H. Ma, X. Liu, S. Inalegwu Okopi, L. Che, Q. Zhang, Z. Sun, F. Xu, Enhanced reductive catalytic fractionation of lignocellulose using a water-resistant RuNiZnOx/Nb2O5 catalyst with synergistic hydrogen spillover and acidic properties, Fuel 373 (2024) 132297, https://doi.org/10.1016/j.fuel.2024.132297.
[17] M. Zhao, J. Hu, S. Wu, L. Yang, X. An, P. Yuan, P. Lu, Hydrodeoxygenation of lignin-derived phenolics over facile prepared bimetallic RuCoNx/NC, Fuel 308 (2022) 121979, https://doi.org/10.1016/j.fuel.2021.121979.
[18] K.B. Jung, J. Lee, J.-M. Ha, H. Lee, D.J. Suh, C.-H. Jun, J. Jae, Effective hydrodeoxygenation of lignin-derived phenols using bimetallic RuRe catalysts: effect of carbon supports, Catal. Today 303 (2018) 191–199, https://doi.org/10.1016/j.cattod.2017.07.027.
[19] S. Echeandia, P.L. Arias, V.L. Barrio, B. Pawelec, J.L.G. Fierro, Synergy effect in the HDO of phenol over Ni–W catalysts supported on active carbon: effect of tungsten precursors, Appl. Catal. B Environ. 101 (2010) 1–12, https://doi.org/10.1016/j.apcatb.2010.08.018.
[20] I. Mudi, A. Hart, A. Ingram, J. Wood, Catalytic Hydrodeoxygenation of Vanillin, a bio-oil model compound over renewable ni/biochar catalyst, Catalysts 13 (2023) 171, https://doi.org/10.3390/catal13010171.
[21] W. Song, Y. Liu, E. Baráth, C. Zhao, J.A. Lercher, Synergistic effects of Ni and acid sites for hydrogenation and C–O bond cleavage of substituted phenols, Green. Chem. 17 (2015) 1204–1218, https://doi.org/10.1039/C4GC01798F.
[22] X. Li, L. Chen, G. Chen, J. Zhang, J. Liu, The relationship between acidity, dispersion of nickel, and performance of Ni/Al-SBA-15 catalyst on eugenol hydrodeoxygenation, Renew. Energy 149 (2020) 609–616, https://doi.org/10.1016/j.renene.2019.12.094.
[23] S. Tieuli, P. Mäki-Arvela, M. Peurla, K. Eränen, J. Wärnå, G. Cruciani, F. Menegazzo, D.Yu Murzin, M. Signoretto, Hydrodeoxygenation of isoeugenol over Ni-SBA-15: kinetics and modelling, Appl. Catal. A Gen. 580 (2019) 1–10, https://doi.org/10.1016/j.apcata.2019.04.028.
[24] X. Wang, Z. Zhang, Z. Yan, Q. Li, C. Zhang, X. Liang, Synergistic contribution of metal–acid sites in selective hydrodeoxygenation of biomass derivatives over Cu/CoOx catalysts, J. Colloid Interface Sci. 648 (2023) 1–11, https://doi.org/10.1016/j.jcis.2023.05.207.
[25] Z. Zhang, X. Wang, C. Wang, Z. Yan, G. Zhuang, N. Ma, Q. Li, Selective hydrodeoxygenation of bio-oil model compounds and mixtures over CuCoOx catalysts under mild conditions, Chem. Eng. J. 483 (2024) 149367, https://doi.org/10.1016/j.cej.2024.149367.
[26] P. Sangnikul, C. Phanpa, R. Xiao, H. Zhang, P. Reubroycharoen, P. Kuchonthara, T. Vitidsant, A. Pattiya, N. Hinchiranan, Role of copper- or cerium-promoters on NiMo/γ-Al2O3 catalysts in hydrodeoxygenation of guaiacol and bio-oil, Appl. Catal. A Gen. 574 (2019) 151–160, https://doi.org/10.1016/j.apcata.2019.02.004.
[27] Q. Peng, X. Jiang, G. Cao, T. Xie, Z. Jin, L. Xie, F. Gan, S. Ma, M. Peng, Selective production of high-value fuel via catalytic upgrading of bio-oil over nitrogen-doped carbon-alumina hybrid supported cobalt catalysts, Bioresour. Technol. 406 (2024) 131059, https://doi.org/10.1016/j.biortech.2024.131059.
[28] D.S. Leite, G.B. Strapasson, D. Zanchet, Unveiling the effect of metallic and oxidized phases of cobalt on acetone hydrodeoxygenation, Mol. Catal. 530 (2022) 112623, https://doi.org/10.1016/j.mcat.2022.112623.
[29] Y. Tian, B. Chen, Z. Yu, R. Huang, G. Yan, Z. Li, Y. Sun, S. Yang, X. Tang, L. Lin, X. Zeng, Efficient catalytic hydrogenation of furfural over cobalt-based catalysts with adjustable acidity, Chem. Eng. Sci. 270 (2023) 118527, https://doi.org/10.1016/j.ces.2023.118527.
[30] C. Lindfors, P. Mäki-Arvela, P. Paturi, A. Aho, K. Eränen, J. Hemming, M. Peurla, D. Kubička, I.L. Simakova, D.Yu Murzin, Hydrodeoxygenation of Isoeugenol over Ni- and Co-Supported Catalysts, ACS Sustain. Chem. Eng. 7 (2019) 14545–14560, https://doi.org/10.1021/acssuschemeng.9b02108.
[31] C. Wen, M. Lu, M. Zhao, J. Zhu, M. Li, J. Shang, Y. Shan, C. Song, Co-based catalysts supported on ceria with different shape structures for hydrodeoxygenation of guaiacol, Energy Fuels 36 (2022) 14986–14993, https://doi.org/10.1021/acs.energyfuels.2c02913.
[32] K.-L. Lu, F. Yin, X.-Y. Wei, J.-H. Li, Z. Li, Z.-C. Fan, Z.-M. Zong, Promotional effect of metallic Co and Fe on Ni-based catalysts for *p*-cresol deoxygenation, Fuel 321 (2022) 124033, https://doi.org/10.1016/j.fuel.2022.124033.
[33] Z. Vajglová, B. Gauli, P. Mäki-Arvela, I.L. Simakova, N. Kumar, K. Eränen, T. Tirri, R. Lassfolk, M. Peurla, D.E. Doronkin, D.Yu Murzin, Co-processing of fossil feedstock with lignin-derived model compound isoeugenol over Fe-Ni/H-Y-5.1 catalysts, J. Catal. 421 (2023) 101–116, https://doi.org/10.1016/j.jcat.2023.03.016.
[34] Z. Vajglová, B. Gauli, P. Mäki-Arvela, N. Kumar, K. Eränen, J. Wärnå, R. Lassfolk, I. L. Simakova, I.P. Prosvirin, M. Peurla, J.K.M. Lindén, H. Huhtinen, P. Paturi, D. E. Doronkin, D.Yu Murzin, Interactions between iron and Nickel in Fe–Ni Nanoparticles on Y zeolite for Co-processing of fossil feedstock with lignin-derived isoeugenol, ACS Appl. Nano Mater. 6 (2023) 10064–10077, https://doi.org/10.1021/acsanm.3c00620.

[35] Z. Vajglová, O. Yevdokimova, A. Medina, K. Eränen, T. Tirri, J. Hemming, J. Lindén, I. Angervo, P. Damlin, D.E. Doronkin, P. Mäki-Arvela, D. Yu. Murzin, Solventless hydrodeoxygenation of isoeugenol and dihydroeugenol in batch and continuous modes over a zeolite-supported FeNi catalyst, Sustain. Energy Fuels 7 (2023) 4486–4504, https://doi.org/10.1039/D3SE00371J.
[36] N.T.T. Tran, Y. Uemura, S. Chowdhury, A. Ramli, Vapor-phase hydrodeoxygenation of guaiacol on Al-MCM-41 supported Ni and Co catalysts, Appl. Catal. A Gen. 512 (2016) 93–100, https://doi.org/10.1016/j.apcata.2015.12.021.
[37] O.B. Ayodele, Influence of oxalate ligand functionalization on Co/ZSM-5 activity in Fischer Tropsch synthesis and hydrodeoxygenation of oleic acid into hydrocarbon fuels, Sci. Rep. 7 (2017) 10008, https://doi.org/10.1038/s41598-017-09706-z.
[38] B.Pratap Singh, G.Sunil More, R. Bal, R. Srivastava, The cooperative effect of Co and CoO in Co/CoO enabled efficient catalytic hydrogenation and demethoxylation of guaiacol to cyclohexanol, Sustain. Energy Fuels 8 (2024) 2153–2166, https://doi.org/10.1039/D4SE00183D.
[39] X. Qu, S. Zhang, J. Mao, H. Lv, J. Zhou, Core–shell structured cobalt oxide nanoparticles and single Co atoms supported on graphene for selective hydrodeoxygenation of syringol to cyclohexanol, Catal. Sci. Technol. 14 (2024) 3382–3395, https://doi.org/10.1039/D4CY00295D.
[40] S. Xiang, L. Dong, Z.-Q. Wang, X. Han, L.L. Daemen, J. Li, Y. Cheng, Y. Guo, X. Liu, Y. Hu, A.J. Ramirez-Cuesta, S. Yang, X.-Q. Gong, Y. Wang, A unique Co@CoO catalyst for hydrogenolysis of biomass-derived 5-hydroxymethylfurfural to 2,5-dimethylfuran, Nat. Commun. 13 (2022) 3657, https://doi.org/10.1038/s41467-022-31362-9.
[41] Daily Metal Price: Cobalt Price (USD / Kilogram) Chart for the Last Max, (n.d.). ⟨https://www.dailymetalprice.com/metalpricecharts.php?c=co&u=kg&d=0⟩ (accessed October 20, 2025).
[42] R. Ahishakiye, F. Wang, X. Zhang, M. Sun, Y. Zhai, Y. Liu, Y. Wu, M. Li, M. Li, Q. Zhang, Novel noble metal-free and recyclable Co-CoOx-FeNiCo/γ-Al2O3 catalyst for selective hydrogenation of 5-hydroxymethylfurfural to 2,5-dimethylfuran or 2,5-Bis(hydroxymethyl)furan, Chem. Eng. J. 450 (2022) 138187, https://doi.org/10.1016/j.cej.2022.138187.
[43] S. Cheng, L. Wei, J. Julson, M. Rabnawaz, Upgrading pyrolysis bio-oil through hydrodeoxygenation (HDO) using non-sulfided Fe-Co/SiO2 catalyst, Energy Convers. Manag. 150 (2017) 331–342, https://doi.org/10.1016/j.enconman.2017.08.024.
[44] T.M. Sankaranarayanan, A. Berenguer, C. Ochoa-Hernández, I. Moreno, P. Jana, J. M. Coronado, D.P. Serrano, P. Pizarro, Hydrodeoxygenation of anisole as bio-oil model compound over supported Ni and Co catalysts: effect of metal and support properties, Catal. Today 243 (2015) 163–172, https://doi.org/10.1016/j.cattod.2014.09.004.
[45] J. Qi, X. Sun, S.-F. Tang, Y. Sun, C. Xu, X. Li, X. Li, Integrated study on the role of solvent, catalyst and reactant in the hydrodeoxygenation of eugenol over nickel-based catalysts, Appl. Catal. A Gen. 535 (2017) 24–31, https://doi.org/10.1016/j.apcata.2017.01.020.
[46] L. Bomont, M. Alda-Onggar, V. Fedorov, A. Aho, J. Peltonen, K. Eränen, M. Peurla, N. Kumar, J. Wärnå, V. Russo, P. Mäki-Arvela, H. Grénman, M. Lindblad, D. Yu Murzin, Production of cycloalkanes in hydrodeoxygenation of isoeugenol over Pt- and Ir-modified bifunctional catalysts, Eur. J. Inorg. Chem. 2018 (2018) 2841–2854, https://doi.org/10.1002/ejic.201800391.
[47] B. Liang, P. Zhu, J. Gu, W. Yuan, B. Xiao, H. Hu, M. Rao, Advancing adsorption and separation with modified SBA-15: a comprehensive review and future perspectives, Molecules 29 (2024) 3543, https://doi.org/10.3390/molecules29153543.
[48] M. Shakeri, Z. Khatami Shal, P. Van Der Voort, An overview of the challenges and progress of synthesis, characterization and applications of plugged SBA-15 materials for heterogeneous catalysis, Materials 14 (2021) 5082, https://doi.org/10.3390/ma14175082.
[49] C. Ziejewska, A. Grela, M. Łach, J. Marczyk, N. Hordyńska, M. Szechyńska-Hebda, M. Hebda, Eco-friendly zeolites for innovative purification of water from cationic dye and heavy metal ions, J. Clean. Prod. 406 (2023) 136947, https://doi.org/10.1016/j.jclepro.2023.136947.
[50] T. Cordero-Lanzac, J. Rodríguez-Mirasol, T. Cordero, J. Bilbao, Advances and Challenges in the Valorization of Bio-Oil: hydrodeoxygenation using carbon-supported catalysts, Energy Fuels 35 (2021) 17008–17031, https://doi.org/10.1021/acs.energyfuels.1c01700.
[51] V. Ranaware, D. Verma, R. Insyani, A. Riaz, S.Min Kim, J. Kim, Highly-efficient and magnetically-separable ZnO/Co@N-CNTs catalyst for hydrodeoxygenation of lignin and its derived species under mild conditions, Green. Chem. 21 (2019) 1021–1042, https://doi.org/10.1039/C8GC03623C.
[52] Z. Li, Z. Li, M. Wu, Z. Qiu, Y. Zhu, R. Zhang, Selective hydrodeoxygenation of lignin-derived eugenol to propylcyclohexane over triazine polymer derived Co/NC-T catalyst, Mol. Catal. 557 (2024) 113987, https://doi.org/10.1016/j.mcat.2024.113987.
[53] E. Blanco, D. Carrales-Alvarado, A. Belen Dongil, N. Escalona, Effect of the support functionalization of mono- and bimetallic Ni/Co supported on graphene in hydrodeoxygenation of guaiacol, Ind. Eng. Chem. Res. 60 (2021) 18870–18879, https://doi.org/10.1021/acs.iecr.1c03073.
[54] W. Chen, Z. Zhang, Y. Ma, X. Dai, R. Wang, Y. Chen, C. Xiong, Y. Luo, X. Li, H. Chang, Pt-based carbon fiber catalytic dehydrogenation of methylcyclohexane in a fixed-bed reactor, Energy Fuels 39 (2025) 2834–2842, https://doi.org/10.1021/acs.energyfuels.4c05756.
[55] J. Lee, K.-H. Kim, E.E. Kwon, Biochar as a Catalyst, Renew. Sustain. Energy Rev. 77 (2017) 70–79, https://doi.org/10.1016/j.rser.2017.04.002.
[56] R. Zou, M. Qian, C. Wang, W. Mateo, Y. Wang, L. Dai, X. Lin, Y. Zhao, E. Huo, L. Wang, X. Zhang, X. Kong, R. Ruan, H. Lei, Biochar: From by-products of agro-industrial lignocellulosic waste to tailored carbon-based catalysts for biomass thermochemical conversions, Chem. Eng. J. 441 (2022) 135972, https://doi.org/10.1016/j.cej.2022.135972.
[57] M. Saidi, F. Samimi, D. Karimipourfard, T. Nimmanwudipong, B.C. Gates, M. Reza Rahimpour, Upgrading of lignin-derived bio-oils by catalytic hydrodeoxygenation, Energy Environ. Sci. 7 (2014) 103–129, https://doi.org/10.1039/C3EE43081B.
[58] J.L. Santos, P. Mäki-Arvela, J. Wärnå, A. Monzón, M.A. Centeno, D.Yu Murzin, Hydrodeoxygenation of vanillin over noble metal catalyst supported on biochars: Part II: Catalytic behaviour, Appl. Catal. B Environ. Energy 268 (2020) 118425, https://doi.org/10.1016/j.apcatb.2019.118425.
[59] G.-H. Liu, Z.-M. Zong, Z.-Q. Liu, F.-J. Liu, Y.-Y. Zhang, X.-Y. Wei, Solvent-controlled selective hydrodeoxygenation of bio-derived guaiacol to arenes or phenols over a biochar supported Co-doped MoO2 catalyst, Fuel Process. Technol. 179 (2018) 114–123, https://doi.org/10.1016/j.fuproc.2018.05.035.
[60] R. Shu, H. Jiang, L. Xie, X. Liu, T. Yin, Z. Tian, C. Wang, Y. Chen, Efficient hydrodeoxygenation of lignin-derived phenolic compounds by using Ru-based biochar catalyst coupled with silicotungstic acid, Renew. Energy 202 (2023) 1160–1168, https://doi.org/10.1016/j.renene.2022.11.092.
[61] P. Parthasarathy, T. Al-Ansari, H.R. Mackey, K. Sheeba Narayanan, G. McKay, A review on prominent animal and municipal wastes as potential feedstocks for solar pyrolysis for biochar production, Fuel 316 (2022) 123378, https://doi.org/10.1016/j.fuel.2022.123378.
[62] Z. Liu, F.-S. Zhang, J. Wu, Characterization and application of chars produced from pinewood pyrolysis and hydrothermal treatment, Fuel 89 (2010) 510–514, https://doi.org/10.1016/j.fuel.2009.08.042.
[63] J. Alvarez, G. Lopez, M. Amutio, J. Bilbao, M. Olazar, Physical activation of rice husk pyrolysis char for the production of high surface area activated carbons, Ind. Eng. Chem. Res. 54 (2015) 7241–7250, https://doi.org/10.1021/acs.iecr.5b01589.
[64] M. Kwiatkowski, E. Broniek, An analysis of the porous structure of activated carbons obtained from hazelnut shells by various physical and chemical methods of activation, Colloids Surf. A Physicochem. Eng. Asp. 529 (2017) 443–453, https://doi.org/10.1016/j.colsurfa.2017.06.028.
[65] D. Baldassin, L. Longo, F. Menegazzo, C. Bittencourt, M. Padervand, M. Signoretto, Co-pyrolysis of leather shaving waste and rice husk for hybrid palladium-supported biochar catalysts in hydrogenation reactions, Mater. Today Sustain. 31 (2025) 101127, https://doi.org/10.1016/j.mtsust.2025.101127.
[66] A.N.M.R. Bin Rahman, J. Zhang, Trends in rice research: 2030 and beyond, Food Energy Secur. 12 (2023) e390, https://doi.org/10.1002/fes3.390.
[67] K. Kuligowski, A. Cenian, I. Konkol, L. Świerczek, K. Chojnacka, G. Izydorczyk, D. Skrzypczak, P. Bandrów, Application of leather waste fractions and their biochars as organic fertilisers for ryegrass growth: agri-environmental aspects and plants response modelling, Energies 16 (2023) 3883, https://doi.org/10.3390/en16093883.
[68] A.Mohan Verma, N. Kishore, Gas phase conversion of eugenol into various hydrocarbons and platform chemicals, RSC Adv. 7 (2017) 2527–2543, https://doi.org/10.1039/C6RA26357G.
[69] Y. Elkasabi, C.A. Mullen, Progress on biobased industrial carbons as thermochemical biorefinery coproducts, Energy Fuels 35 (2021) 5627–5642, https://doi.org/10.1021/acs.energyfuels.1c00182.
[70] X. Liu, L. Xu, G. Xu, W. Jia, Y. Ma, Y. Zhang, Selective Hydrodeoxygenation of Lignin-Derived Phenols to Cyclohexanols or Cyclohexanes over Magnetic CoNx@NC Catalysts under Mild Conditions, ACS Catal. 6 (2016) 7611–7620, https://doi.org/10.1021/acscatal.6b01785.
[71] T. Lear, R. Marshall, J. Antonio Lopez-Sanchez, S.D. Jackson, T.M. Klapötke, M. Bäumer, G. Rupprechter, H.-J. Freund, D. Lennon, The application of infrared spectroscopy to probe the surface morphology of alumina-supported palladium catalysts, J. Chem. Phys. 123 (2005) 174706, https://doi.org/10.1063/1.2101487.
[72] X. Tang, Z. Jiang, Z. Li, Z. Gao, Y. Bai, S. Zhao, J. Feng, The effect of the variation in material composition on the heterogeneous pore structure of high-maturity shale of the Silurian Longmaxi formation in the southeastern Sichuan Basin, China, J. Nat. Gas. Sci. Eng. 23 (2015) 464–473, https://doi.org/10.1016/j.jngse.2015.02.031.
[73] R. Nava, B. Pawelec, P. Castaño, M.C. Álvarez-Galván, C.V. Loricera, J.L.G. Fierro, Upgrading of bio-liquids on different mesoporous silica-supported CoMo catalysts, Appl. Catal. B Environ. 92 (2009) 154–167, https://doi.org/10.1016/j.apcatb.2009.07.014.
[74] D.D. Purkayastha, B. Sarma, C.R. Bhattacharjee, Surfactant-assisted low-temperature synthesis of monodispersed phase pure cubic CoO solid nanoparallelepipeds via thermal decomposition of cobalt(II) acetylacetonate, Mater. Lett. 107 (2013) 71–74, https://doi.org/10.1016/j.matlet.2013.05.122.
[75] V.A. de la Peña O'Shea, P.R. de la Piscina, N. Homs, G. Aromí, J.L.G. Fierro, Development of hexagonal closed-packed cobalt nanoparticles stable at high temperature, Chem. Mater. 21 (2009) 5637–5643, https://doi.org/10.1021/cm900845h.
[76] M.C. Biesinger, B.P. Payne, A.P. Grosvenor, L.W.M. Lau, A.R. Gerson, R.St. C. Smart, Resolving surface chemical states in XPS analysis of first row transition metals, oxides and hydroxides: Cr, Mn, Fe, Co and Ni, Appl. Surf. Sci. 257 (2011) 2717–2730, https://doi.org/10.1016/j.apsusc.2010.10.051.
[77] Q. Guo, J. Mao, S. Li, J. Yin, Y. Lv, J. Zhou, Cobalt–graphene catalyst for selective hydrodeoxygenation of guaiacol to cyclohexanol, Nanomaterials 12 (2022) 3388, https://doi.org/10.3390/nano12193388.
[78] M. Si, S. Wang, X. Gou, H. Song, Co doping induces CoxP-Ni2P bimetallic site and acid synergistic effect to achieve efficient hydrodeoxidation, J. Fuel Chem. Technol. 52 (2024) 1327–1335, https://doi.org/10.1016/S1872-5813(24)60477-9.

[79] M. Liu, J. Zhang, L. Zheng, G. Fan, L. Yang, F. Li, Significant promotion of surface oxygen vacancies on bimetallic CoNi nanocatalysts for hydrodeoxygenation of biomass-derived vanillin to produce methylcyclohexanol, ACS Sustain. Chem. Eng. 8 (2020) 6075–6089, https://doi.org/10.1021/acssuschemeng.0c01015.
[80] B.P. Singh, G.S. More, R. Bal, R. Srivastava, The cooperative effect of Co and CoO in Co/CoO enabled efficient catalytic hydrogenation and demethoxylation of guaiacol to cyclohexanol, Sustain. Energy Fuels 8 (2024) 2153–2166, https://doi.org/10.1039/D4SE00183D.
[81] S. Li, B. Liu, J. Truong, Z. Luo, P.C. Ford, M.M. Abu-Omar, One-pot hydrodeoxygenation (HDO) of lignin monomers to C9 hydrocarbons co-catalysed by Ru/C and Nb 2 O 5, Green. Chem. 22 (2020) 7406–7416, https://doi.org/10.1039/D0GC01692F.
[82] M.-Y. Chen, Y.-B. Huang, H. Pang, X.-X. Liu, Y. Fu, Hydrodeoxygenation of lignin-derived phenols into alkanes over carbon nanotube supported Ru catalysts in biphasic systems, Green. Chem. 17 (2015) 1710–1717, https://doi.org/10.1039/C4GC01992J.
[83] C. Zhao, J. He, A.A. Lemonidou, X. Li, J.A. Lercher, Aqueous-phase hydrodeoxygenation of bio-derived phenols to cycloalkanes, J. Catal. 280 (2011) 8–16, https://doi.org/10.1016/j.jcat.2011.02.001.
[84] P. Zhang, W. Duan, H. Peng, B. Pan, B. Xing, Functional biochar and its balanced design, ACS Environ. Au 2 (2022) 115–127, https://doi.org/10.1021/acsenvironau.1c00032.
[85] M. Zhang, S. Chi, H. Huang, Y. Yu, Mechanism insight into MnO for CO activation and O removal processes on Co(0001) surface: a DFT and kMC study, Appl. Surf. Sci. 567 (2021) 150854, https://doi.org/10.1016/j.apsusc.2021.150854.
[86] X. Liu, W. Jia, G. Xu, Y. Zhang, Y. Fu, Selective hydrodeoxygenation of lignin-derived phenols to cyclohexanols over Co-based catalysts, ACS Sustain. Chem. Eng. 5 (2017) 8594–8601, https://doi.org/10.1021/acssuschemeng.7b01047.
[87] D.Yu Murzin, J. Wärnå, H. Haario, T. Salmi, Parameter estimation in kinetic models of complex heterogeneous catalytic reactions using Bayesian statistics, Reac Kinet. Mech. Cat. 133 (2021) 1–15, https://doi.org/10.1007/s11144-021-01974-1.
[88] A. Bjelić, M. Grilc, B. Likozar, Catalytic hydrogenation and hydrodeoxygenation of lignin-derived model compound eugenol over Ru/C: intrinsic microkinetics and transport phenomena, Chem. Eng. J. 333 (2018) 240–259, https://doi.org/10.1016/j.cej.2017.09.135.
[89] T. Cordero-Lanzac, I. Hita, A. Veloso, J.M. Arandes, J. Rodríguez-Mirasol, J. Bilbao, T. Cordero, P. Castaño, Characterization and controlled combustion of carbonaceous deactivating species deposited on an activated carbon-based catalyst, Chem. Eng. J. 327 (2017) 454–464, https://doi.org/10.1016/j.cej.2017.06.077.
[90] M. Shetty, D. Zanchet, W.H. Green, Y. Román-Leshkov, Cooperative Co0/coii sites stabilized by a perovskite matrix enable selective C−O and C−C bond hydrogenolysis of oxygenated arenes, ChemSusChem 12 (2019) 2171–2175, https://doi.org/10.1002/cssc.201900664.